Title
On the Gular Sac Tissue of the Brown Pelican: Structural Characterization and Mechanical Properties

Author
Dike, Seth Conlan

Publication Date
2019

UNIVERSITY OF CALIFORNIA SAN DIEGO

On the Gular Sac Tissue of the Brown Pelican: Structural Characterization and Mechanical Properties

A Thesis submitted in partial satisfaction of the requirements

for the degree of Master of Science

in

Engineering Sciences (Mechanical Engineering)

by

Seth Conlan Dike

Committee in charge:

Professor Marc A. Meyers, Chair
Professor Shengqiang Cai
Professor Joanna M. McKittrick

2019

The Thesis of Seth Conlan Dike is approved, and it is acceptable in quality and form for publication on microfilm and electronically:

Chair

University of California San Diego

2019

Table of Contents

Signature Page iii

Table of Contents iv

List of Figures vi

List of Tables x

Acknowledgements xi

Abstract of the Thesis xii

1 Introduction 1

2 Methods and materials 6

2.1 Preparation of skin for tensile testing 6

2.2 Preparation of skin for observation 11

2.2.1 Environmental scanning electron microscopy 11

2.2.2 Transmission electron microscopy 12

2.2.3 Ultra-high resolution scanning electron microscopy 13

3 Results and discussion 15

3.1 Microstructure 15

3.1.1 Transmission electron microscopy 15

3.1.2 Scanning electron microscopy 22

    - 3.1.3 Ultra-high resolution scanning electron microscopy 25
  - 3.2 Age and Anisotropy 29
  - 3.3 Constant strain rate 41
  - 3.4 Property variance by location 47
    - 3.4.1 Proximal variation 48
    - 3.4.2 Dorsoventral variation 52
- 4 Conclusions 64
- 5 Appendix: MANOVA results for dorsoventral data 66
- References 69

List of Figures

Figure 1: Depiction of the similarities of feeding mechanics between pelicans and rorqual whales (Balaenopteridae) 4

Figure 2: Left: Reuge strain equivalency in tensile tests [7]. Right: Field rorqual-pelican tensile dataset. 5

Figure 3: Two immature and an adult brown pelican (10). 6

Figure 4: Illustrates process of separating the sample space from the carcass. 7

Figure 5: Transverse specimen prior to testing (a) and fully extended just prior to failure (b). 9

Figure 6: Transverse specimen post-fracture. This specimen broke at the gage length's midpoint despite the presence of sharp shoulder geometries. 10

Figure 7: Location map for TEM samples. 11

Figure 8: Fibril image selections of the transverse cross-section. 15

Figure 9: Analysis of fibril size. 17

Figure 10: Bimodal plot of fibril diameters seen in transverse orientation. 18

Figure 11: Fibril width, (center). Fiber width (right), showing the fibrils making up the fiber. 19

Figure 12: Rabbit fibers and fibrils imaged by TEM and SEM, adapted from [8] images collagen fibrils microstructure and fiber macrostructure for rabbits. 21

Figure 13: Schematic of a 3-layer structure consisting of skeletal muscle and SSE (stratified squamous epithelium) 23

Figure 14: ESEM of fracture surfaces and mandible-gular sac interface. 24

Figure 15: Connection of gular skin to the mandible. 25

Figure 16. Images of fiber bundles' curvature and sheet-like microstructure. 27

Figure 17: Closer view of SEM image showing areas from which curvature of bundles is estimated. 28

Figure 18: Even closer view of Figure 16. 28

Figure 19: Comparison of pig [9] (top) and pelican (lower) radii of collagen fibers. 29

Figure 20: Magnification of the corrugated groove structure and splitting of the two layers of skin. 31

Figure 21: Diagram of the corrugated groove structure of the gular sac 32

Figure 22: Comparison of pelicans 1, 2, 4, and 5 in representative parameters by orientation... 36

Figure 23: Description of regions in a typical skin response curve and depiction of fibril alignment during deformation. 37

Figure 24: Comparison of pelicans 1 and 5 in terms of sample orientation. 38

Figure 25: Comparison of pelicans 2 and 4 in terms of sample orientation. 39

Figure 26: Juvenile (one to three years old) pelican 4's map of sample orientation. 40

Figure 27: Adult (more than 3 years old) pelican 5's map of sample orientation. 40

Figure 28: Distribution of heel and linear region attributes by constant strain rate for Pelican 1. 42

Figure 29: Pelican 1's average tensile curves for strain rates spanning two orders of magnitude. 42

Figure 30: Comparison of longitudinal specimens of rabbit skin and pelican gular skin at strain rates of 10^{-1} and 10^{-3} s^{-1}. 45

Figure 31: Comparison of transverse specimens of rabbit skin and pelican gular skin at strain rates of 10^{-1} and 10^{-3} s^{-1}. 46

Figure 32: Comparison of pig and pelican maximum stress and strain at failure [9]. 47

Figure 33: Pelican 1's proximal study with heel region attributes and strain energy. 48

Figure 34: Pelican 2's distribution for proximal variation. 51

Figure 35: Pelican 2's results for proximal variation in longitudinal and transverse orientations. 52

Figure 36: Pelican 4's map of region tagging for dorsoventral variation. 53

Figure 37: Pelican 2 and 5's maps of region tagging for dorsoventral variation. 54

Figure 38: Comparison of pelicans 2 (a), 4 (b), and 5 (c) for dorsoventral variation in the transverse orientation 56

Figure 39: Comparison of pelicans 2 (a), 4 (b), and 5 (c) for dorsoventral variation in the longitudinal orientation 57

Figure 40: Comparison of dorsoventral regions 60

Figure 41: The fifth pelican's 'axis' region consists of a thicker line of collagen along the pouch base. 61

Figure 42: Heel slope scatter charts. 66

Figure 43: Heel slope scatter plot for location after grouping bulk and axis locations. 67

Figure 44: Scatter plots for heel intercept. All P-values were less than 0.001. 67

Figure 45: Scatter plots for linear slope. P-orientation < 0.001, P-location < 0.001, and P-age = 0.0024. 67

Figure 46: Scatter plots for linear intercept. All P-values < 0.001. 68

Figure 47: Scatter plots for maximum stress. P-orientation < 0.001, P-location < 0.001, P-age = 0.308. 68

Figure 48: Scatter plots for strain at maximum stress. All P-values < 0.001. 68

Figure 49: Scatter plots for strain energy. P-orientation < 0.001, P-location < 0.164, and P-age = 0.038. 68

List of Tables

Table 1: Comparative values in fibril and fiber microstructure for the pig, rabbit, and pelican.. 20

Table 2: Description of all pelicans involved in this study. Blue rows indicate maturity. 33

Table 3: Comparison of the experimental values for pelicans 1, 2, 4, and 5. 37

Table 4: Multiple regression analysis of the influence of sample orientation, specimen location, and pelican age (estimated) on heel slope, heel intercept, linear slope, linear intercept, maximum stress, strain at maximum stress, strain energy. 63

Acknowledgements

Special thanks to Professor Marc A. Meyers for his guidance and support during my course of study and research at U.C. San Diego and for being the chair of my committee.

I would like to thank Professors Cai and McKittrick for being on my committee as well.

I would like to acknowledge Philip Unitt for arranging the transfer of the first pelican carcass from Project Wildlife contact Maria Gonzalez.

I would like to acknowledge the following affiliates at SeaWorld–San Diego for contributing the remaining six pelicans. Dr. Judy St. Leger organized the collaborative research agreement under which Kaylin Ackerson and Alexandria Mena handled the storage of birds.

The method of TEM preparation detailed in Section 2.2.2 was provided by Mason Mackey, who tailored the process to best preserve the microstructure of pelican skin. Haocheng Quan assisted with multiple rounds of TEM preparation, and performed the imaging.

Dr. Wen Yang prepared all SEM specimens and performed multiple rounds of imaging. Her insight was key to understanding the separation of layers and attachment to the mandible. The methods for ESEM and UHR-SEM preparation, and she provided Sections 2.2.1 and 2.2.3. She additionally assisted with the preparation and tensile experimentation of several carcasses.

I would like to acknowledge Andrei Pissarenko for guidance in TEM post-processing. He also advised on selection of experimental parameters, resulting in trends across the deformation regions.

This work was partially funded by a Multi-University Research Initiative (grant no. AFOSR-FA9550-15-1-0009) from the Air Force Office of Scientific Research to the University of California Riverside, through subcontracts to the University of California, San Diego and the University of California, Berkeley.

ABSTRACT OF THE THESIS

On the Gular Sac Tissue of the Brown Pelican:

Structural Characterization and Mechanical Properties

by

Seth Conlan Dike

Master of Science in Engineering Sciences (Mechanical Engineering)

University of California San Diego, 2019

Professor Marc A. Meyers, Chair

Although the Brown Pelican wields one of the largest bills of any bird, it is distinguished by the deployable throat pouch of extensible tissue used to ‘net’ prey. Researchers have primarily focused on the bending mechanics that pelican bills demonstrate during feeding. While the mandible’s ability to endure hydrodynamic loading during plunge-diving has been reported on, little has been published on the pouch itself in the form of gular sac tissue characterization.

This thesis reports on mechanical testing and optical characterization of the pouch material, similar in scope and methods to recent studies at UCSD involving pig and rabbit skin. The data suggests a higher extensibility of the pelican skin to the pig using a limited comparison of fibril curvatures. TEM imaging provides microstructural evidence of the directionality of the collagen fibers. This, paired with the corrugated nature of the pouch material in the circumferential or expansive direction, elicits the anisotropic response observed in tensile testing. TEM also showed the dimensions of collagen fibrils to be similar in size to those in rabbits and pigs—suggesting the fibrils themselves are likely not the main reason for the enhanced extensibility observed beyond other skin types. Material characterization efforts focused on the impact of the following parameters: relative bird age, location on the pouch, and constant strain rate. Anteroposterior location and strain rate were not yet determined major influencers on exhibited strengths and extensibilities. However, bird age and dorsoventral location were found to affect the pouch material's mechanical response significantly.

1 Introduction

Efforts to understand the unique features possessed by the pelican family began with the tracking of advantageous traits and study of how species converge. Through this, researchers happened upon a beak structure already fully optimized to handle dorsoventral bending stresses thrust upon it. Field compares the feeding mechanics exhibited by rorqual whales and pelicans, developing flexural rigidity distributions for the lower mandibles as evidence of their similarities [1]. Scaled to the anatomical proportions of the whale, pelican jaws actually outperform whale jaws in settings of pure bending. Rorqual mandibles must sacrifice geometry advantageous to bending resistance to manage other substantial loadings, like torsion, brought on by jaw operation at such an immense scale. Field attributes the fluctuation in lower jaw rigidity to variation in bone density in an earlier publication, reporting more porous cross-sections towards the anterior, or outer end [2]. Campbell-Malone describes such a pattern as contradictory to the porosity trends exhibited by most whales and closely-related sea birds, such as the cormorant; the engulfment feeding actions of the rorquals and pelicans must then account for this [3].

Field's team began their study of pelican beaks by highlighting the difference in beak structure between pelican species. While brown and white pelicans are analogous in patterns of flexural rigidity, the levels of rigidity differ. This disparity was speculated to arise from differences in feeding styles [1]. Since browns plunge as deep as 16 meters to feed, their mandibles must endure high bending stresses further elevated by rapid pouch inflation at these depths. American White pelicans prefer to scan the water's surface for movement, then quickly snatch up prey swimming near the surface.

Considering the following interpretation, mandibles as cantilever beams and water as uniform loading, Vogel describes an increase in flexural rigidity in the posterior direction—towards the cranial joint—mirroring the trend of dorsoventral stress [4]. Bending resistance is maximized at the site of muscle attachment, where the lower mandible has a nearly elliptical cross-section. Vogel further examines the utility provided by this shape, suggesting that the geometry contributes to both the outward bowing of mandibles and existence of an optimized rigidity to the original direction of loading. The ellipse's major axes run the dorsoventral direction to provide the necessary bending resistance. The minor axes of the mandible contain less material, signifying a lower moment of inertia and preferential direction of deformation. The bowing behavior allows for deflection of loading into the mediolateral plane, alleviating a considerable portion of dorsoventral bending stresses [4]. Myers and Meyers refer to the action of actively bowing mandibles outwards as streptognathism [5]. This outward flexing of the beak provides a wide framework, enabling the rapid inflation of a pouch to its maximum volume. Stiffness trends in the dorsoventral and mediolateral planes were compared in terms of deflection. Field found that mandibles loaded dorsoventrally are eight times more resistant to bending than those tested in the mediolateral direction [1]. Background of the pelican's beak deflection is integral to study of the gular sac tissue since beak and pouch mechanics are interrelated.

Field's team published the first paper examining the gular sac's mechanical properties, characterizing the material for resistance to hydrodynamic loading and experienced pressures in dragging for prey [1]. Potvin reports the contents of the rorquals' ventral groove blubber (VGB) as an intermediate muscle layer sandwiched between collagen [6]. This central muscle tier is thought to limit the rate of pouch expansion, providing some extent of control to water level in the pouch. Field suggests gular sac tissue to be similar in structure – and that the elastic properties exhibited are defined by the behaviour of collagen fibres [1]. Figure 1 provides a side-by-side comparison of the species' expansive tissue. The pelican's pouch material was classified as anisotropic – three times more extensible in the transverse, or dorsoventral direction, than in the longitudinal, or anterior-posterior direction. Transverse pouch skin stretches when low pressures are applied, but begins to stiffen as collagen fibers straighten and align. The longitudinal orientation does not share the same extensibility; fibers are already aligned with the testing direction.

Using biaxial bubble inflation pioneered by Reuge, the central sac region was tested in the form of 5 cm aperture samples over multiple inflation pressures [7]. Field describes the rorqual whale ventral groove blubber (VGB) - and pelican gular skin - as anisotropic [1]. This assertion is only supported by two instances of the biaxial bubble test, producing a total of four tensile curves: two for longitudinal (parallel with groove lines), two for transverse (perpendicular to groove lines). While these experiments appear almost identical for each orientation, there is simply not enough information to quantitatively define the properties of the material. Reuge attempts to correlate the tensile curves obtained through uniaxial and biaxial arrangements [7]. Figure 2 shows the strain equivalency for either method of tensile as charted by Reuge. This is paired with Field's rorqual whale and pelican tensile data, tested by uniaxial and biaxial means, respectively. While soft tissues favor biaxial arrangements in the determination of realistic models of anisotropic materials, this study does not consider these values as a valid comparison to the material following characterization. Although the whale tensile testing was performed with uniaxial arrangements, as is all of the following data contained in this thesis, the testing orientation is not provided so there can be no meaningful relation between the evolutionary converged materials.

Figure 1: Depiction of the similarities of feeding mechanics between pelicans and rorqual whales (Balaenopteridae) . Top left [12] and bottom images: pelicans showing prominent dark groove lines along gular skin. Middle: whale with ventral groove blubber (VGB) at full expansion [13].

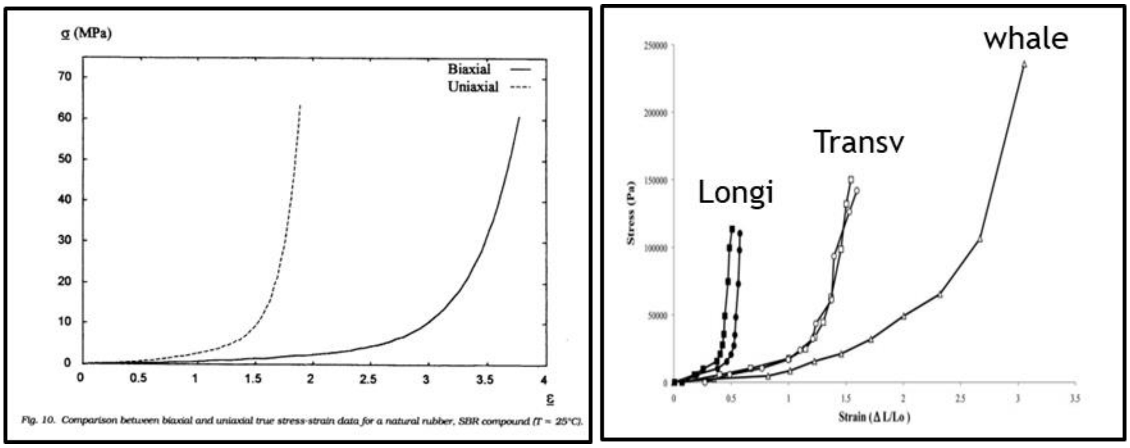

Figure 2: Left: Reuge strain equivalency in tensile tests [7]. Right: Field rorqual-pelican tensile dataset. Note the whale curve is uniaxial and the individual pelican orientations are derived from a biaxial experiment.

With the acquisition of birds from SeaWorld, we began establishing a database of information about the gular skin of the brown pelican. This includes characterization of the material under the following parameters: relative age of bird, proximity to mandibles (dorsoventral variation), proximity to the neck (anteroposterior variation), and variation of strain rate. Additionally, each pelican's uniaxial tensile dataset supports the earlier suggestion of anisotropy though the pouches of the youngest birds were nearly isotropic. Parameters found to influence the properties, such as dorsoventral variation and bird age, were further studied. SEM usage focused on the interface of bill and gular skin. TEM provided visual verification of the likely microstructural sources of the observed anisotropy, and was used to determine that the collagen fibrils are consistent with data published for rabbit and pig skin.

2 Methods and materials

2.1 Preparation of skin for tensile testing

Pelican pouches were acquired from two sources. The San Diego Natural History Museum generously provided the first fresh pelican carcass. The following six pelicans were released from SeaWorld - San Diego. Although the majority of birds received were infants, or less than a year old, there were a few mature adults, over three-years old, in the mix. See Figure 3 for differences in plumage indicative of age. Collaborators at SeaWorld narrate the plumage's transition with age as: "*juveniles less than 1 year have a boring, brown head. Between 2-3 years the head is speckled brown-white. By the time the bird is 3 years, it will have beautiful solid white head plumage.*" The grooves on the pouch's exterior become more prominent and defined; their coloration begins as a mossy green and saturates with age into a near black shade.

Figure 3: Two immature and an adult brown pelican (10).

The process of preparing tensile specimens began with removal of the pouch's sample space from attachment along the lower neck and beak. To measure properties most representative of a live bird, samples were cut, beginning at the beak tip and ending at the lower throat. By drawing from the sample space nearest the tip, skin can remain attached to the carcass longer, remaining moist and slowing the decay of these experimental parameters. However, this method did not make efficient use of the pouch's sampleable space. From the second bird onwards, the method was modified, practicing a full removal of the sample space. This allowed for the optimal mapping of potential specimen locations and equal assignment of testing orientations. Occasional misting with DI water helped limit dehydration of the skin. Figure 4 illustrates the creation of a bird's sample space, also dictating the grooving association to discussed testing orientations.

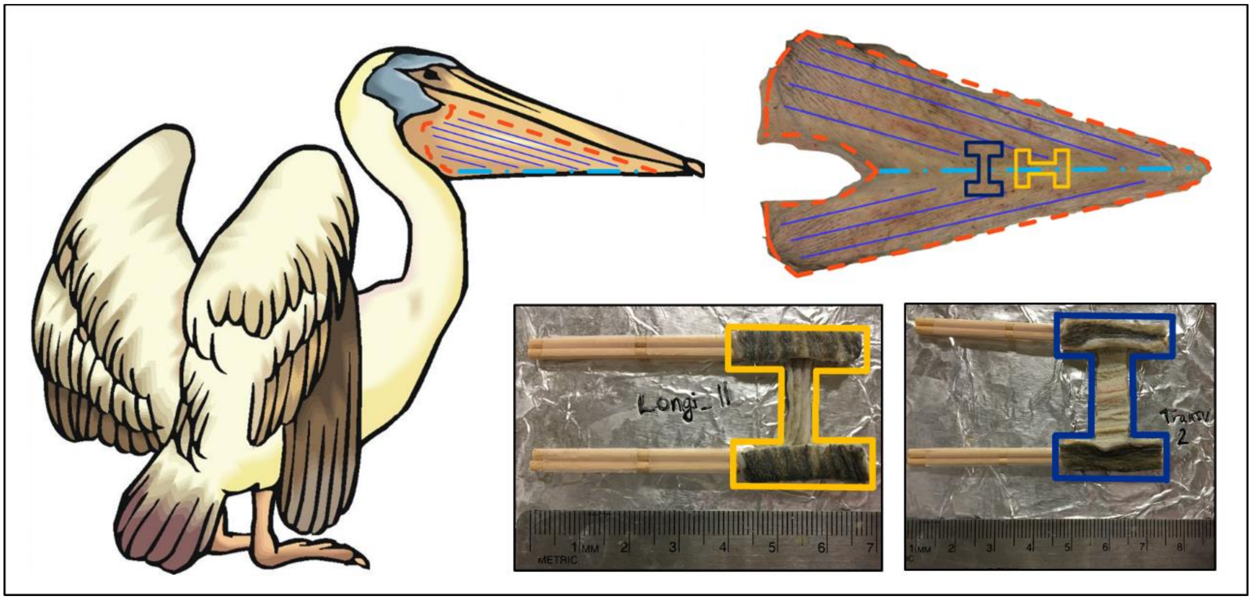

Figure 4: Illustrates process of separating the sample space from the carcass.

Four pelicans were devoted to exploration of parameters of interest, attempting to draw causality between significance tensile results and observed trends in behavior. Each carcass pouch contributed 24 - 30 tensile specimens, maintaining a relatively even split between testing orientations. Testing of each bird pouch was continuous and uninterrupted—specimens belonging to the same bird should have no variability due to experimental environment. Figure 4 also introduces the ‘dog-bone’ shape consistent in all tensile experiments performed. To reduce skin slippage inside the gripping jaws, the wider ends of the sample were wrapped around a pair of toothpicks; Loctite 495 adhesive was used to adhere the skin to the wood. Figure 5 shows (a) a specimen ready for testing and (b) fully extended just prior to failure. Figure 6 depicts a transverse sample immediately after fracture. While shoulder-gage angles likely contributed to the generation of stress localization, a fair amount of samples actually broke mid-section of the gage length after less damaging grippers were installed. Gage length was increased from 10 mm to reduce pre-stretch of the specimen before loading. Sample conditioning was not performed due to the difficulty in determining the equilibrium position for soft materials; keeping a consistent initial tension of the sample between the grips is quite challenging. This can possibly attest to the slight delays seen for the start of J-curve responses.

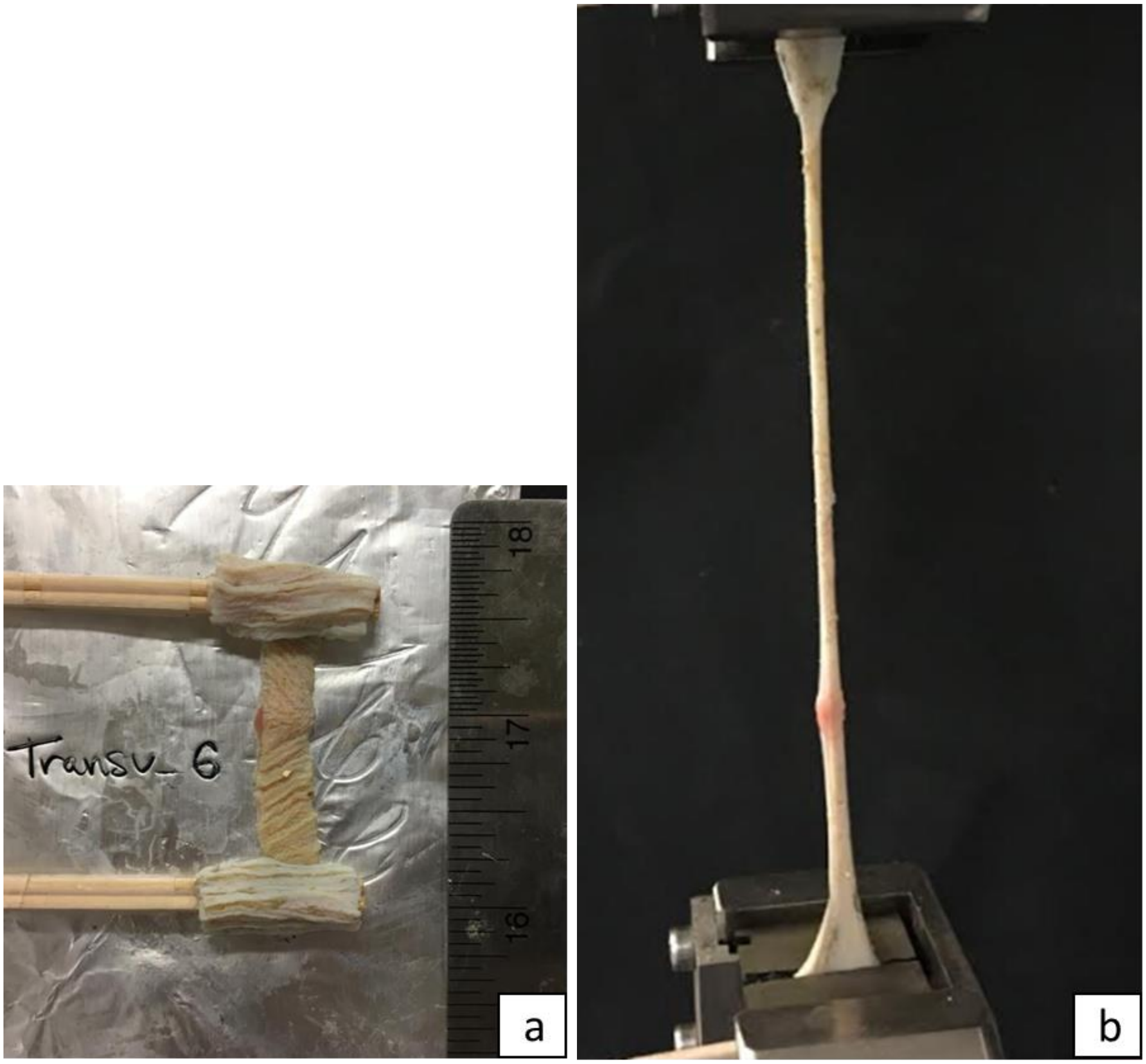

Figure 5: Transverse specimen prior to testing (a) and fully extended just prior to failure (b).

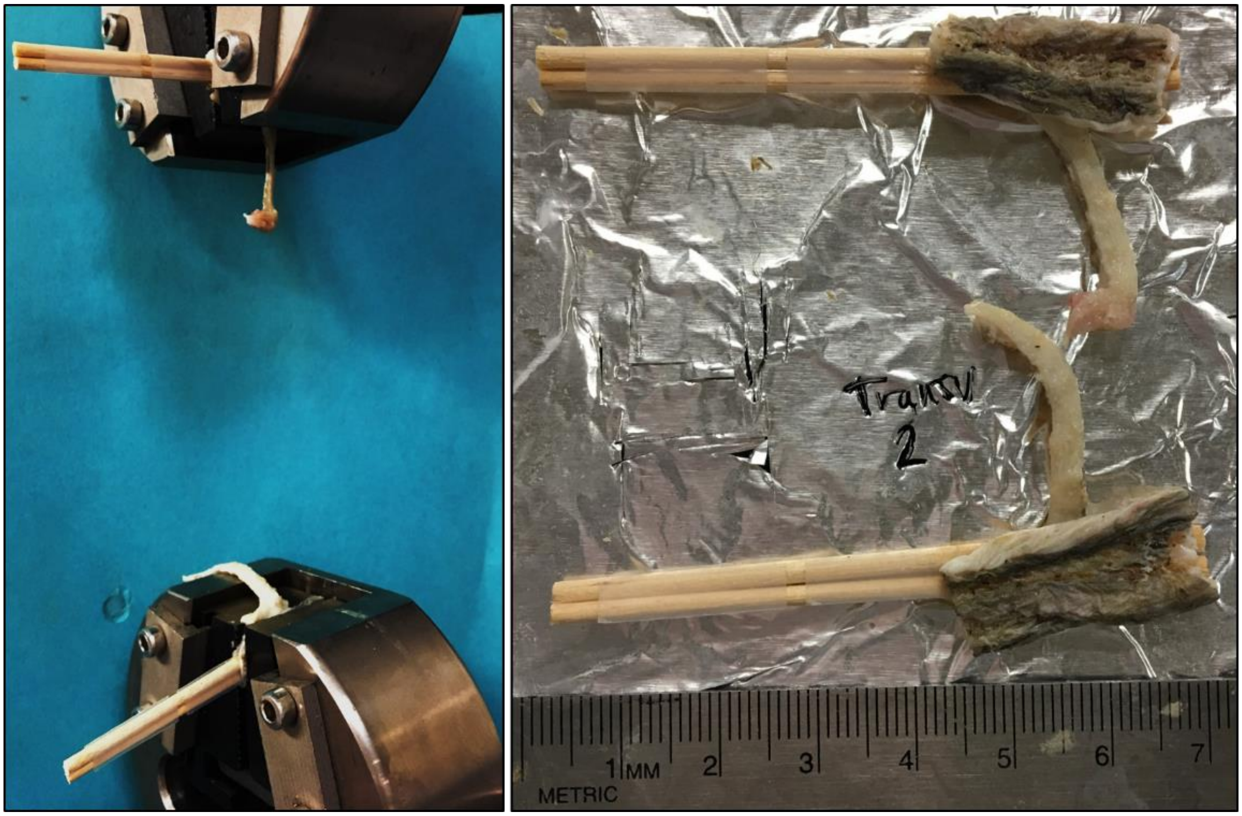

Figure 6: Transverse specimen post-fracture. This specimen broke at the gage length's midpoint despite the presence of sharp shoulder geometries.

Uniaxial tensile tests were performed on an Instron 3342 mechanical testing machine (Instron Corp.) equipped with a 500 N load cell. Specimens were stretched at strain rates of 10^{-3}, 10^{-2}, and 10^{-1} s^{-1}, thus spanning two orders of magnitude, but remaining within machine limitations. The two remaining pelicans were used to explore cyclic loading methods for evaluation of the pelican skin's viscoelastic behavior, or relaxation under periods of stress. Several specimens were given pre-cracks midway up the gage length; however, this notching was done solely to induce sample breakage away from the gripping jaws, in order to produce higher quality fracture surfaces for SEM observation. Pre-cracked sample datasets were not included in the analysis of the skin's properties. This allows us to define the material by its natural response at a cost of additional variability. However, skin specimens were tested ex vivo and carcasses were, in some instances, stored in a freezer for a few days. These conditions do not help to produce the most representative characterization of the tissue. A portion of the gular sacs of these birds was dedicated to the production of TEM and SEM specimens.

2.2 Preparation of skin for observation

Scanning and transmission electron microscopy were used to further support the findings of tensile experiments. Cross-sections of transverse and longitudinal orientations, defined in Figure 7, display the dominant directionality of collagen fibers, thereby acting as visual confirmation to the anisotropy behavior of the pouch. TEM observation also allows comparison of fiber distribution to rabbit and pig skin publications in our group. SEM imaging supports theory that skin bordering the beak differs in properties from 'bulk' region samples. It also provides a three-dimensional glimpse of the skin's layers—how fibers interlace and form sheets.

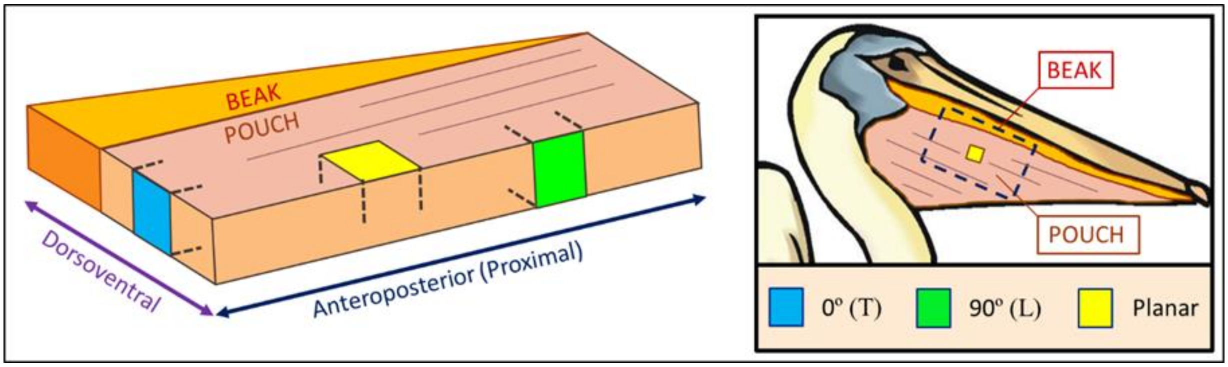

Figure 7: Location map for TEM samples. Blue is transverse (0º). Green is longitudinal (90º). Yellow is planar or the surface of the outside of the pouch.

2.2.1 Environmental scanning electron microscopy

To verify the deformation mechanisms during the tensile test of notched specimens, tension samples with a gauge length of 6 mm and width of 4 mm, were prepared in the longitudinal direction. Uniaxial tension tests were performed at 25ºC in an environmental Hitachi S-4300SE/N

(Hitachi America, Pleasanton, CA) SEM. Testing was performed at a displacement rate of 0.5 mm min^{-1} using a Gatan Microtest 150 N tensile stage (Gatan, Abington, UK) inside the SEM. This testing, however, was used specifically to examine crack deformation and fracture mechanisms associated with the mandible-gular sac interface.

2.2.2 Transmission electron microscopy

Strips of skin for TEM were taken from a freshly thawed pelican throat. Figure 7 indicates the relative locations and orientations of incisions made. Samples required at least one dimension under 1 mm to allow for full penetration of the fixative. Strips of 5 mm x 1 mm were cut and prepped for imaging following the process described by Mason Mackey. The selected tissue was incubated 10 minutes in a pre-warmed fixative, comprised of 2.0% paraformaldehyde, 2.5% glutaraldehyde, and 3 mM $CaCl_2$ in 0.15 M cacodylate buffer (pH 7.4, 37ºC). This mixture was then iced at a temperature of 4ºC overnight. After the fixative was removed, samples underwent a series of washes, 5x15 minutes, using the iced 0.15 M cacodylate buffer and 3 mM $CaCl_2$ (pH 7.4) solution. Next, the tissue was soaked in an iced solution of 1% aqueous osmium tetroxide, 0.15 M cacodylate buffer (pH 7.4), 3 mM $CaCl_2$, and 0.8% potassium ferrocyanide for two hours. This post-fixative was replaced with iced ddH20, or double-distilled water, through a 5x15 minute series of washes. Samples were later incubated overnight in 2% aqueous uranyl acetate, placed in a dark environment at 4ºC. After another 5x15 minute wash series of iced ddH_20, the tissue was dehydrated through an ascending ethanol series, soaked at 20%, 50%, 70%, 90%, and 100% iced solutions for 15 minutes apiece. This was followed by two 100% dry ethanol washes and one wash at a 1:1 ratio of acetone and 100% dry ethanol—using room temperature substances now. While samples sat in a final wash, this time pure acetone, Durcupan ACM resin was prepared. The resin's proper ratio, by mass, is the following: 11.4 g component A, 10 g component B, 0.3 g component C, and 4 drops of component D. After letting the resin set for 20 minutes, the tissue sat in a mixture of 25% Durcupan and 75% acetone for 2 hours. This process was repeated for each stage of an ascending Durcupan series, continued with 50% resin-acetone and 75% resin-acetone mixtures for two hours apiece. Samples were then kept in 100% Durcupan overnight. The following day, the strips received two more soaks of 100% Durcupan, but for two hour intervals. The tissue was delicately removed from vials and placed in numbered 'bullet' molds. Half of the samples were positioned for comparison of fiber directionality in transverse and longitudinal orientations. The others 'bullets' held planar face samples from 'axis' and 'bulk' regions; the purpose of these is to examine the grooved exterior layer of the pouch skin. Molds received 100% Durcupan via eyedropper into the remaining space. Samples were polymerized inside an oven heated to 60ºC over a time period of two days. Upon removal, the castings were sectioned parallel to the exposed skin surface, using a Leica Ultracut UCT ultramicrotome (Leica) and Diatome diamond knife (Diatome) to produce thin films of 70-100 nm thickness. Sections were set on TEM copper grids and finished with Sato lead staining.

2.2.3 Ultra-high resolution scanning electron microscopy

Sections of undeformed pelican skin were immersed in 2.5% glutaraldehyde for 3 h to fix the structure, and subsequently dehydrated with an ascending ethanol series. Strips of skin were cut using a surgical blade. Some samples were fractured by freezing in liquid nitrogen. The samples were then dried in a critical point dryer (Tousimis Auto Samdri 815A). The surfaces were sputter coated with iridium using an Emitech K575X and examined using a FEI SFEG ultra-high resolution SEM. Sections of undeformed pelican skin were immersed in 2.5% glutaraldehyde for 3 hours to fix the structure, immediately after excision or testing. Samples were dehydrated by consecutive immersion in 50%, 70%, 90%, and 100% ethanol solutions. Strips of skin were cut in the cross-section and parallel to the surface of the dermis using a surgical blade. The samples were then dried in a critical point dryer (Tousimis Auto Samdri 815A), and surfaces sputter coated with iridium (Emitech K575X). A FEI SFEG ultra-high resolution SEM was used to visualize the arrangement of the constitutive elements of skin.

3 Results and discussion

3.1 Microstructure

3.1.1 Transmission electron microscopy

Two rounds of samples were prepped for TEM observation. The first set of images contains section-views at the following orientations: 90º (longitudinal), 45º (cross-cut), and 0º (transverse). With the exception of the transverse orientation, this round of imaging did not provide the expected insight. Cross-cut and longitudinal sectioning solely confirm the presence of fiber layers and begin to illustrate the array of fibril directionalities. The image recognition software Fiji (Schindelin & Arganda-Carreras, 2012). ImageJ (Rueden & Schindelin, 2017) was the workhorse used for all image post-processing.

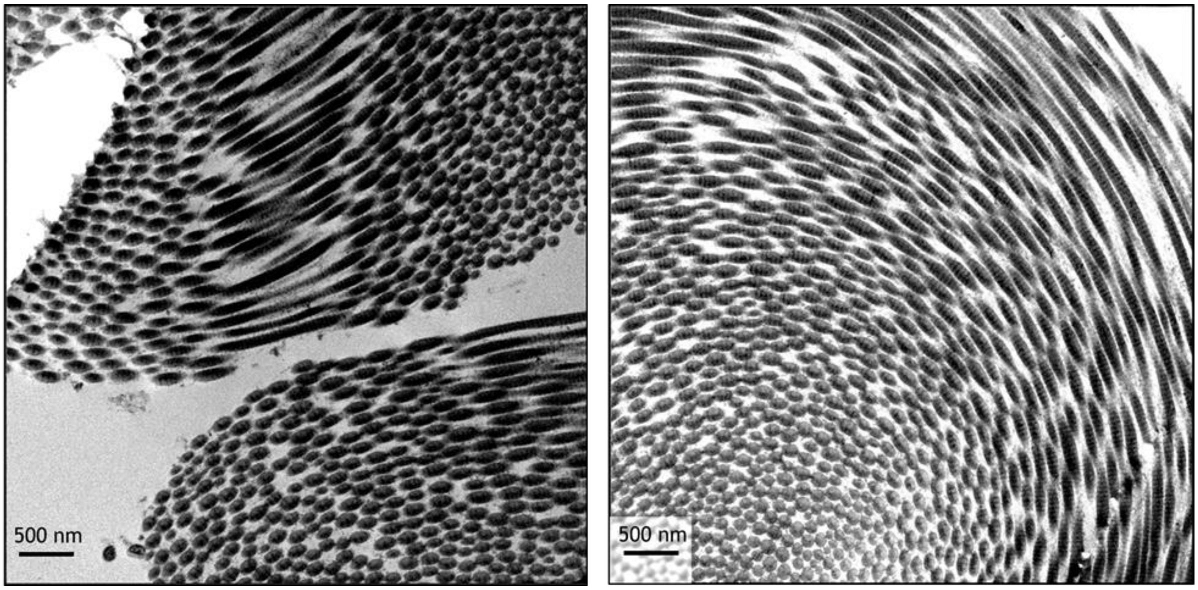

Figure 8: Fibril image selections of the transverse cross-section. .Parallel running bundles are, in this orientation, short out-of-plane bends along the length of longer and predominantly normal running fibrils. TEM performed by Quan, H.

Selected regions from the full image map were edited on an individual basis using contrast, brightness, and binary sensitivity settings in order to enhance image features of interest. Figure 8 depicts several examples of the coiling of collagen fibrils, shown in directions both parallel and normal to the plane. Fiji's feature recognition capability was then used to highlight distinct fibrils using size and circularity filters. Figure 9 provides a glimpse into the editing process. As the settings used to improve the visibility of fibrils varied somewhat for each region, this setting variability could be regarded as a potential source of error. Although the Fiji 'erode' and 'dilate' functions may have affected the diameter~~s~~ measurements, they were necessary for the proper isolation of neighboring fibrils. Circularity and size limits were set to higher values to prevent partially-circular spaces between fibrils from being incorrectly recognized as fibrils. There are two consequences that result from the aggressive levels of these filters. First, it is likely that a number of the smallest diameter fibrils in a given region were not correctly identified. Setting these filters to the higher end of their ranges prevents noise from over-estimating the low-end of fibril diameters. Second, fibrils exceeding size expectations may have been separated into multiple, average-sized fibrils. A cap to the maximum area an individual fibril was used to prevent the assessment of a group of small neighboring fibrils as a single very large fibril. This technique can only provide a probable average; identifying the full spectrum of diameters—the smallest and largest—would either require individual attention and pinpointing of fibrils or further development of a "find-all" method. The difficulty stems from the gradient in fibril sizes seen—a great example of nature's complexities. While such inconsistencies slow the study of biomimicry, they can emerge as the feature that inspires the development of cutting-edge designs and prompts the creation of additional advanced materials.

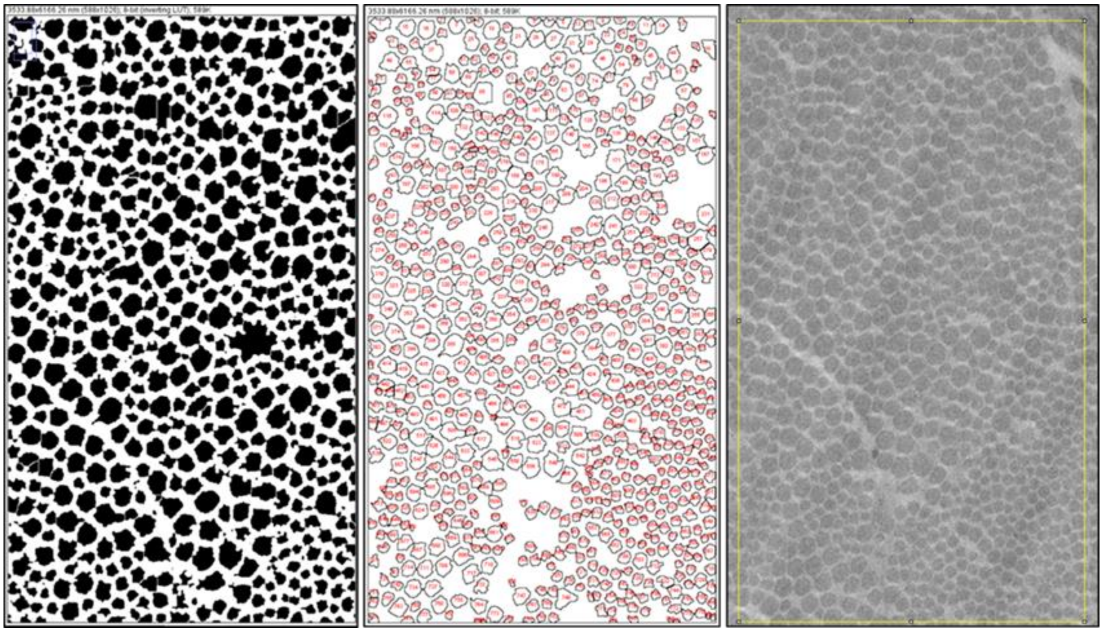

Figure 9: Analysis of fibril size. Recognized fibrils (left). Diameters and circularity of fibrils (center). Original image of transverse orientation edited for brightness and contrast (right).

Figure 10 shows that the average fibril diameters have a bimodal distribution, with fibril diameters centered at 104.6 and 164.8 nm. Although this data does not plot all data together, most regional distributions follow this observed grouping. A few checks were done to verify the reasonableness of these diameters. The number of fibrils identified per sampled area ranged from 213 to 793, and these sampled regions were not all of the same area. Using fibril counts to calculate the weighted average for diameter, mean fibril diameters in the sampled regions were calculated to have diameters of 104.6 and 165.8 nm. The difference in these average values is relatively small compared to the range of diameters measured, indicating a somewhat consistent average fibril size over the sampled region, which is not unexpected. The second check, on the reasonableness of the measured average fibril diameter over the sample space, was intended to assess if the selected region's dimensions influence the fibril quantities identified. The average is weighted using the percentage of fibril coverage developed from recognized diameters and the encompassing region's area. Normally each region being sampled would contain the same sample area, but there are several reasons for the differing sampling sizes. The sample sizes were the result of trying to include as many fibrils as possible in each region's data pool, catering to locations of the map where the fibrils are most clear and discernible. Derived from the counts of fibrils for each sampled regions, diameter sizes were found to peak at 101.4 and 161.8 nm. One difference in the method used for calculation of these average fibril diameters is that for this second estimate of fibril diameters, the region's area estimate includes both fibrils and the space between them. Note that several sampled areas did not produce data indicating a bimodal distribution, but rather a unimodal one that sits almost midway between the two dominant average diameters. These unimodal values were incorporated into the data set of the lowest value, but most frequently occurring, diameter for both checks.

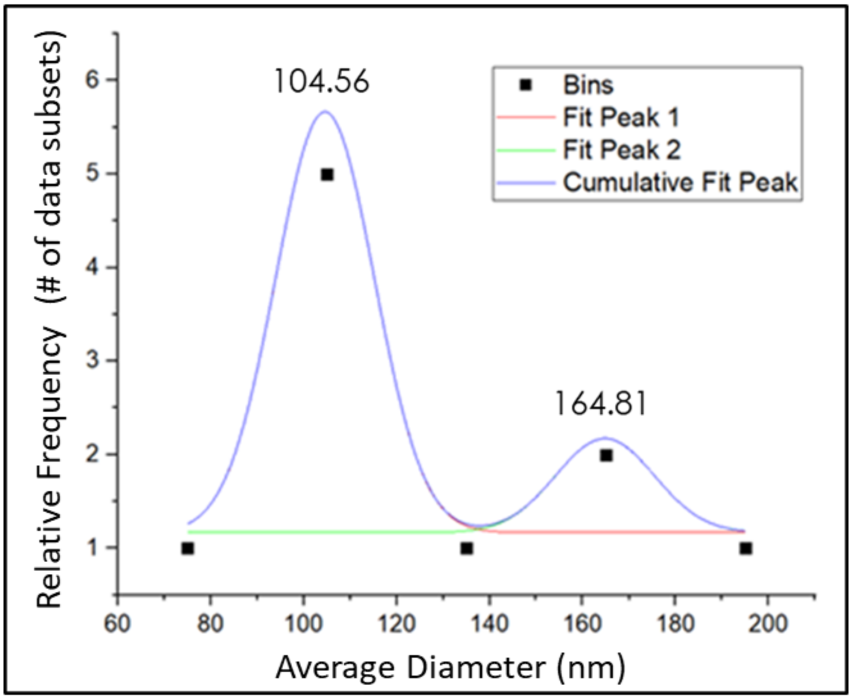

Figure 10: Bimodal plot of fibril diameters seen in transverse orientation.

Figure 11 illustrates the dimensioning process for both fibers and fibrils running parallel to the imaged plane. Fibers appear to be between 2-3 µm in width. However, one particular region acted as an exception, featuring a fiber roughly 6 µm in width. Seeing as how fiber widths in the other five regions were observed to be only half this wide, the 6 µm measurement is likely the result of two layered fibers, pressed up against one another. The parallel fiber sampling regions were reused for fibril width analysis.

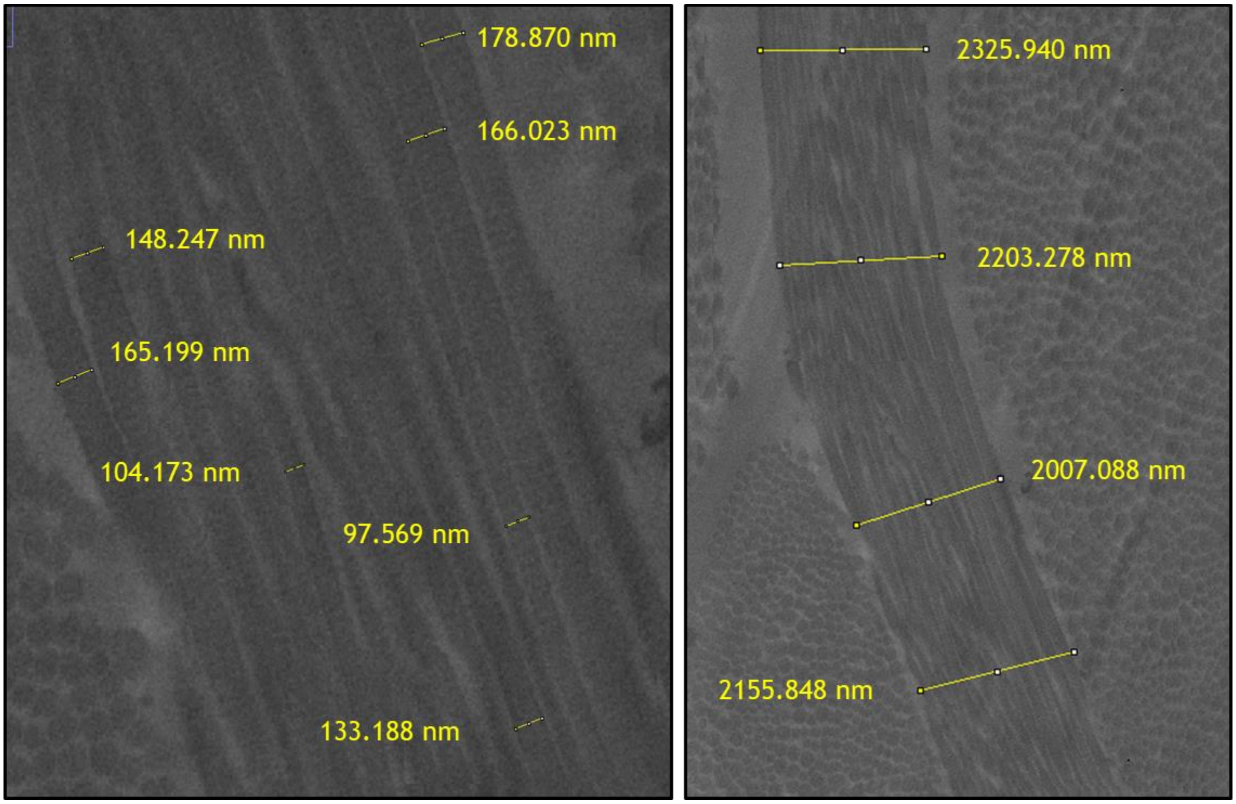

Figure 11: <u>Fibril</u> width, (center). <u>Fiber</u> width (right), showing the fibrils making up the fiber.

Fibril widths were found to also follow a bimodal distribution, favoring diameters of 127.7 and 178.3 nm. Compare this to the dimensions taken from fibrils running normal to the imaged area. Both peaks for the parallel fibril diameter distribution are higher than for those seen in fibrils running normal to the image. One possible explanation for the difference in observed fibril diameter distribution peaks could be that during the post-processing of normal fibrils, the diameter was reduced slightly. This is specifically referencing image recognition software binary settings like ‘erode’. Another possible reason could be that the dimension bars placed across parallel fibrils included small amounts of area tagged as matrix material, or material in between the fibrils. Note that diameters contributed by fibrils running normal to the image area were from a much larger dataset, involving 500-800 fibrils per image selected, than those from images with fibrils running parallel to the image area with 200-793 samples per image.

Table 1 lists all discussed values for fibril and fiber size, comparing them with the data extracted from the referenced rabbit and pig publications. The orientation of the fibers relative to the image areas is also included. Figure 12 presents the origin of the rabbit skin microstructure information [8]. Pig skin data in Table 1 was sourced from Pissarenko [9]. In terms of fiber thickness, rabbits average between 1-2 µm; note these were measured for fibers running parallel with the image area. For pigs, the average value for fiber thickness was 2.2 µm. This measurement from the pelican data was 2-3 µm. Since the values were relatively similar for all animals, the fiber thickness must not be a prominent parameter causing the skin’s exceptional extensibility.

Table 1: Comparative values in fibril and fiber microstructure for the pig, rabbit, and pelican. The additional rows for the normal fibril diameter reference the weighted averages. Blue values are measured running parallel. Orange are measured as normal cross-sections. Note that these values are based off of a bimodal distribution where the first peak is dominant (see Figure 10).

Parameter	Pelican	Pig	Rabbit
Fiber Thickness (µm)	2-3	2.2	1-2
Fibril Diameter (nm)	127.7, 178.3	-	50-100
Fibril Diameter (nm)	104.6, 164.8	82, ~112	-
Fibril Diameter (nm)	104.6, 165.8	Weighted by number of fibrils.	
Fibril Diameter (nm)	101.4, 161.8	Weighted by fibril coverage percentage.	

Source: Pig [9]. Rabbit [8].

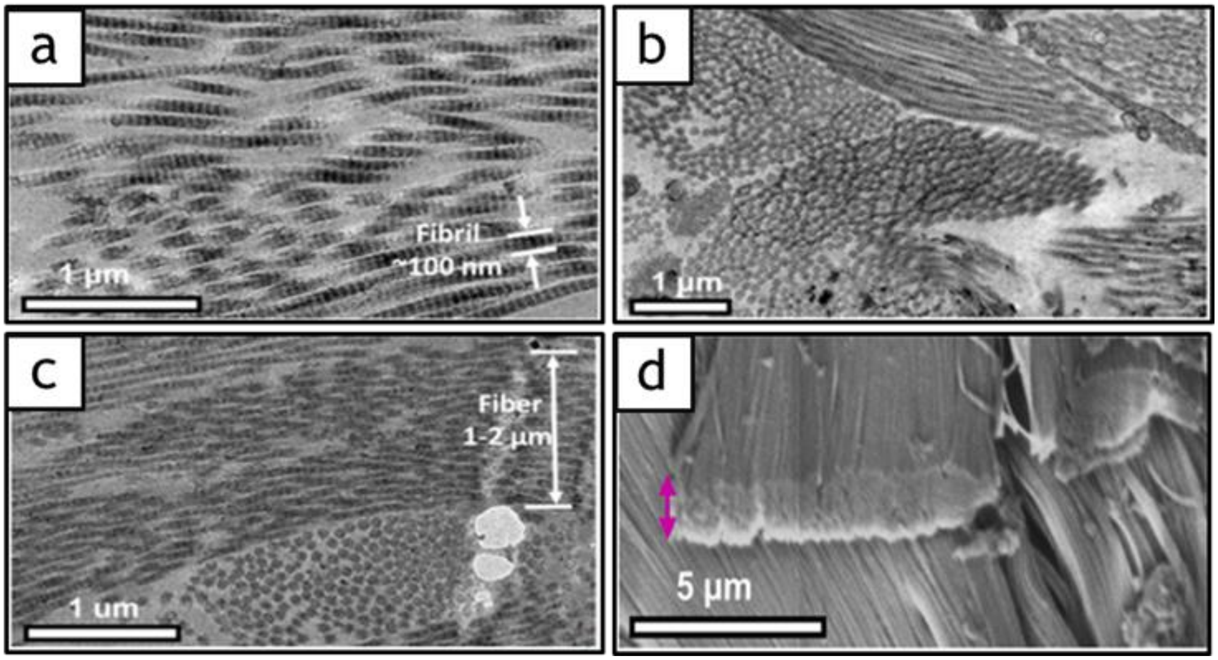

Figure 12: Rabbit fibers and fibrils imaged by TEM and SEM, adapted from [8] images collagen fibrils microstructure and fiber macrostructure for rabbits.

For rabbit fibrils imaged running parallel, common diameters identified lie between 50 and 100 nm [8]. Again, pelican fibrils measured parallel to the image favor modes of 127.7 and 178.3 nm, the former being the dominant peak in the fibril diameter distribution. Values for the pig were measured running normal to the image with peaks in the fibril diameter distributions of 82 nm and secondary at 112 nm. The fibril diameter peak-couple for the pelican, seen with fibrils normal to the image, was 104.6 and 164.8 nm. Each study observed approximately the same principal fibril diameter, converging around 100 nm. The studies do, however, disagree in the way the distributions are skewed. The rabbit fibril diameter distribution was documented to have positive skewness, with numerous diameters observed below the principal. The pelican's secondary data peak rests in the vicinity of 170 nm, showing signs of negative skewing. Despite the variance observed in the distribution's tail, fibril diameters are generally similar in these three animals.

Fibril diameter is then not likely to be a prominent factor in the additional extensibility observed in the pelican gular sac relative to regular skin.

3.1.2 Scanning electron microscopy

Initial understanding of the skin's hierarchy began with a three-layer structure, depicted by Williams as skeletal muscle sandwiched between specialized epidermal layers [10]; see Figure 13. Since possession of this structure may be the enabler of such high extensibility, it is helpful to understand the anatomy of the system. The epidermis, defined specifically as stratified squamous epithelium (SSE), saw no evidence of keratinization for the pelican's gular tissue; this class of tissue typically requires the secretion of bodily fluids to prevent the drying out of cells. The 'stratified' descriptor attests to the arrangement of cells as a multitude of layers. A 'squamous' layer consists of cells that are more compressed, indicative of flatter structures. As SSE undergoes constant abrasion, the dead cells shed form the stratum corneum, or exposed epidermal surface.

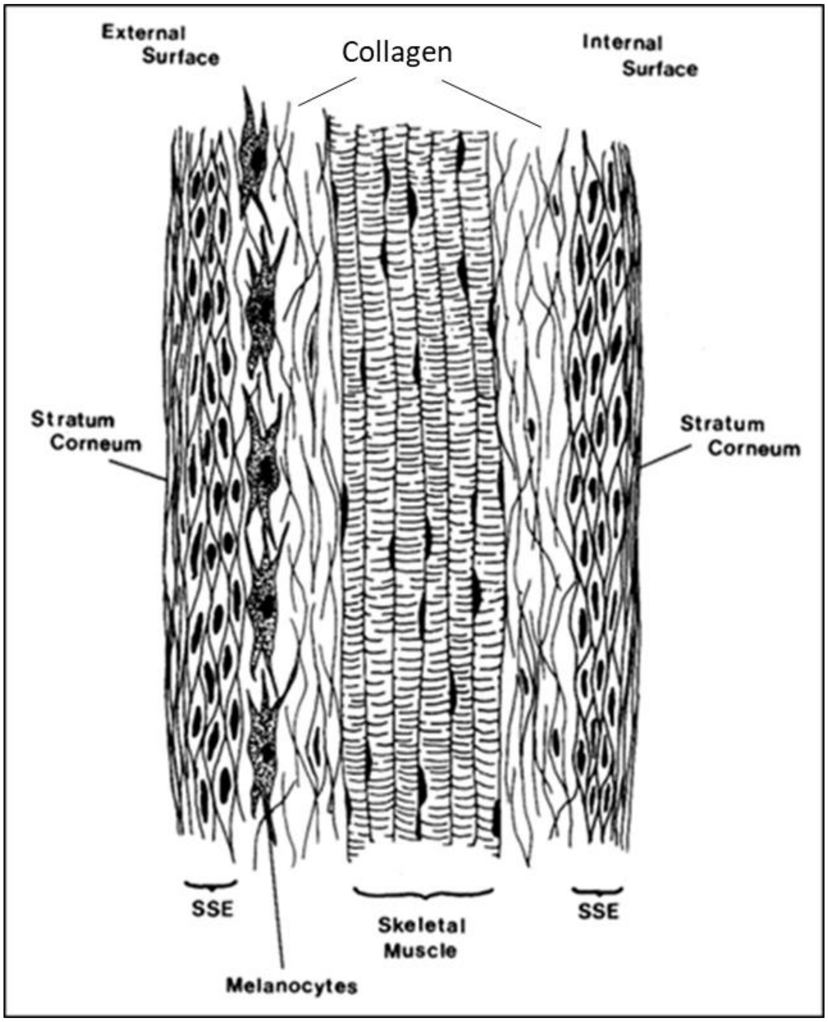

Figure 13: Schematic of a 3-layer structure consisting of skeletal muscle and SSE (stratified squamous epithelium) [10].

SEM was not performed to contend the microstructure at a cellular level, as described by Williams. Rather, the following observations, visible in Figure 14, are directed towards understanding the interface of mandible bone and gular sac tissue. The images reveal a division of skin into two layers where the bone connects. This conflicts with the original statement that gular skin consists of three primary layers. To clarify, there is no challenge to the three layers in terms of biological distinction, but for functionality. It is being suggested that two layers—an exterior and interior each consisting of epidermis and half the muscle—define the operation of the pouch.

Figure 15 highlights the division of layers, proposing that the skeletal muscle interior could be, indeed, two parallel layers. These layers of muscle may be woven together over the bulk of the pouch, but appear to split just before connection to the beak. The alternative possibility is that the gular skin consists of three layers in terms of functionality and biological distinction, and that this hypothesis is wrong. However, this would not explain the gap between the two layers in the muscle near the beak. Going forward, the considered layers will be referred to as exterior and interior.

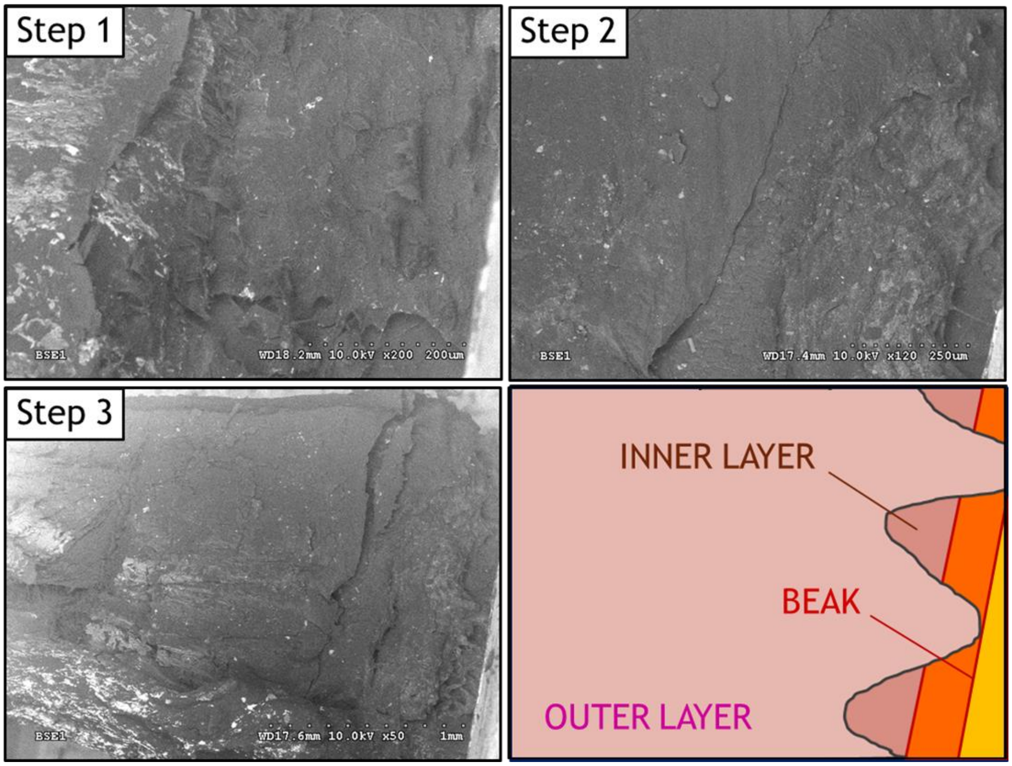

Figure 14: ESEM of fracture surfaces and mandible-gular sac interface. Note the two layers separated near attaachment to the beak. Images were taken by Yang, W.

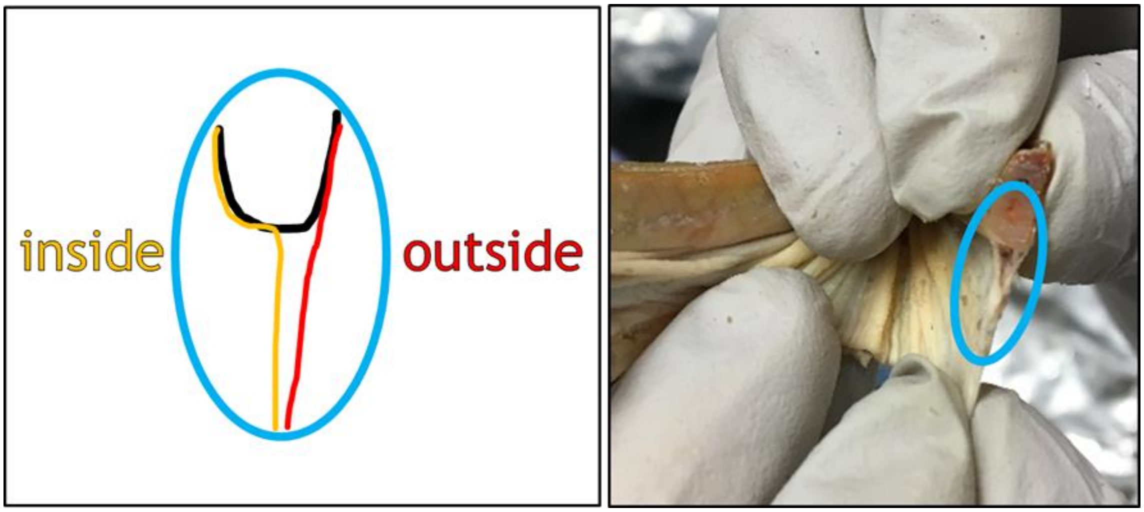

Figure 15: Connection of gular skin to the mandible. This section has been cut to showcase the division of skin layers—not that 'into the page' is towards the beak tip.

Figure 15 also illustrates the attachment of the skin to bone. The inner half of skin appears to follow the mandible's cross-section more significantly than the outer. This means the attainable volume, or amount of space the pouch can contain, is maximized by this configuration. Had the exterior skin followed the beak's cross-sectional curvature all the way to where the inner skin separates from the mandible, the maximum pouch expansion possible would be reduced. The film of gular skin coating the lower mandible differs in properties between exterior and interior locations. The exterior skin shifts to a hard and thin film as it climbs the bone, implying the presence of a mineralization gradient. The inner skin appears to only slightly decrease in thickness, and remains much more compressible and soft. It does, however, also display signs of mineralization but to a lesser extent.

3.1.3 Ultra-high resolution scanning electron microscopy

While the first SEM effort focused on the interface of skin and beak, the second sought to examine the surface of the material in greater detail.

Figure 16 depicts observations from this examination, with (a) providing the larger overview of the skin's thickness. Evidence of keratin in the pouch's exterior and the sheet structure of collagen fibers are shown in (b) and (c), respectively. Recall the SSE in the pelican's gular tissue was not thought include a definitive keratin layering, yet it is present in this image [10]. See images (d) and (e) for a glimpse of fiber curvature and individual fibrils. Wavy collagen fibers stand to be the first possible crimping structure, resulting in such stretchy behaviour. Figure 17 and Figure 18 depict the process of estimating the fibril curvatures. This small sampling is compared with the data from pig in Figure 19 [9]. From this very limited comparison the pelican fibrils appear to be biased toward higher curvature than the pig. This is expected to contribute to the higher extensibility seen in the pelican skin. Pissarenko suggests the fibril bundle's opening angle may act as more of a tell-tale parameter for the material's stretch; this direction will be pursued first in further study of gular sac stretch.

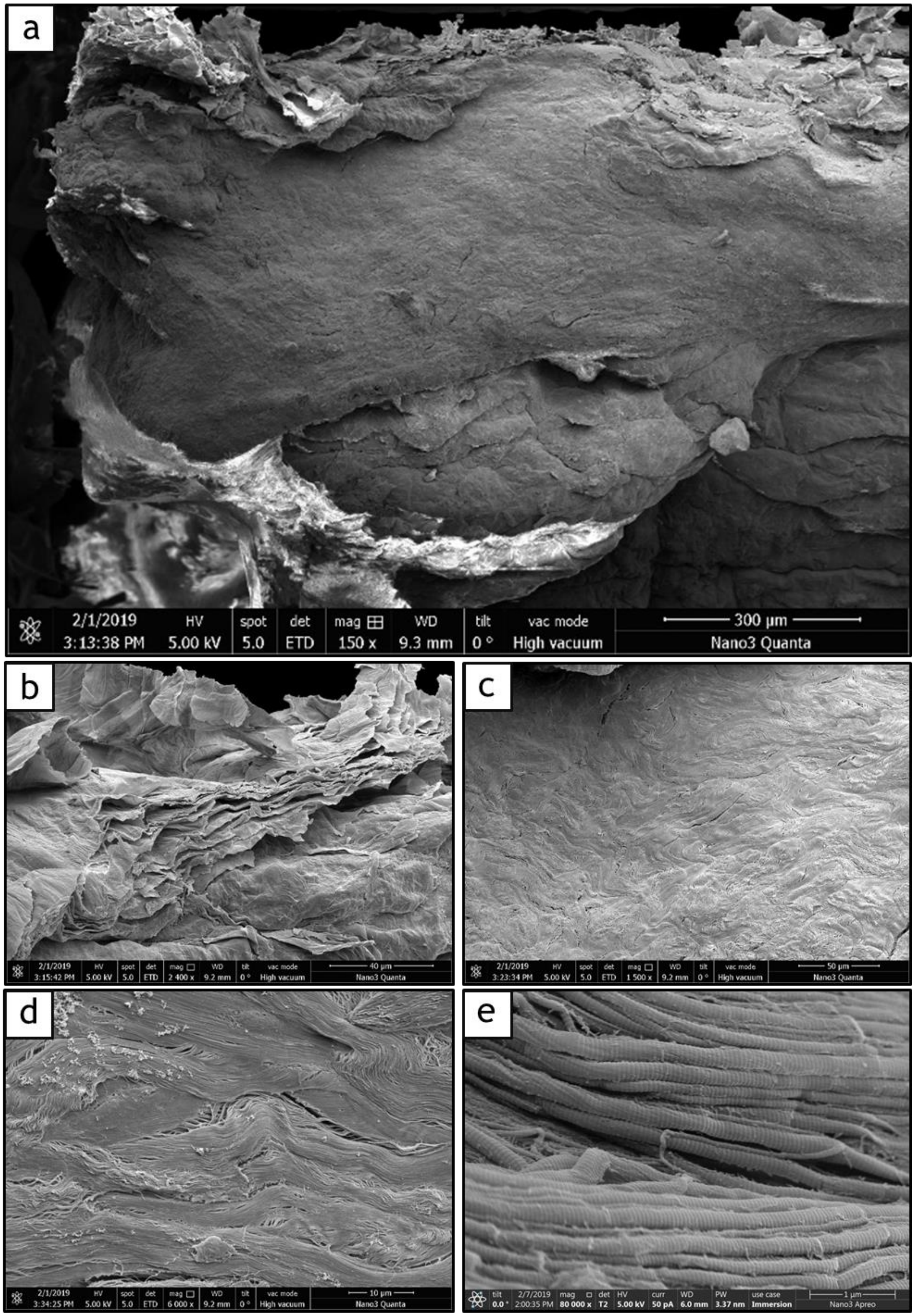

Figure 16. Images of fiber bundles' curvature and sheet-like microstructure. Scales for images are: 300, 40, 50, 10, 50, 1 µm, respectively. HR-SEM performed by W. Yang.

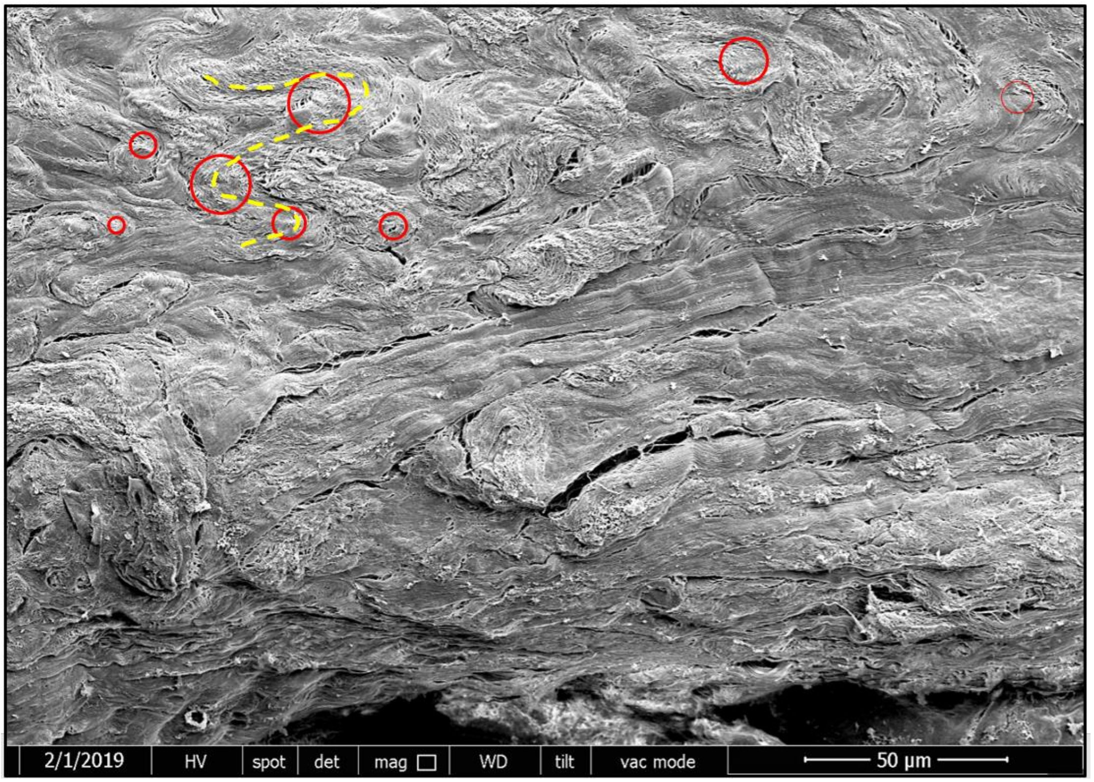

Figure 17: Closer view of SEM image showing areas from which curvature of bundles is estimated.

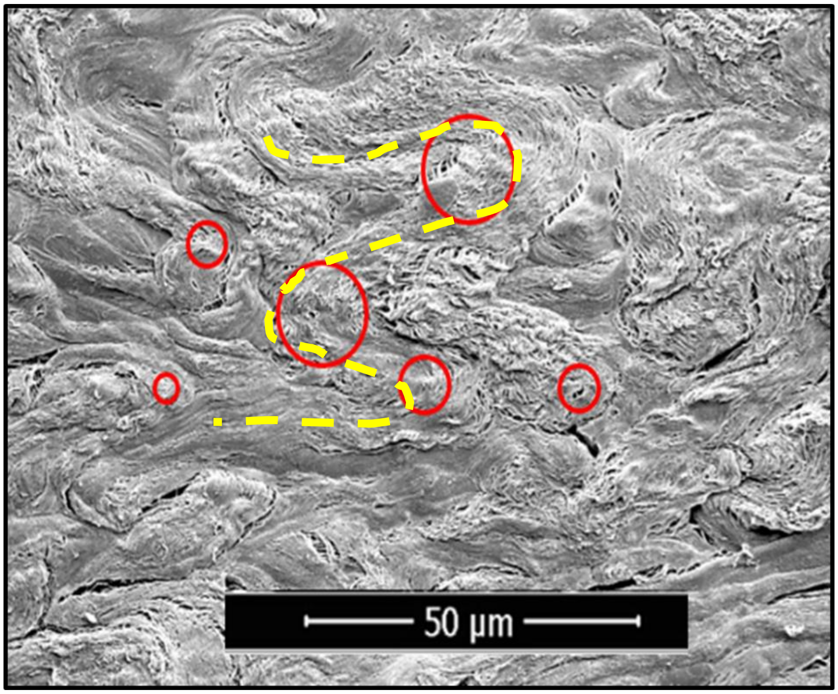

Figure 18: Even closer view of Figure 17.

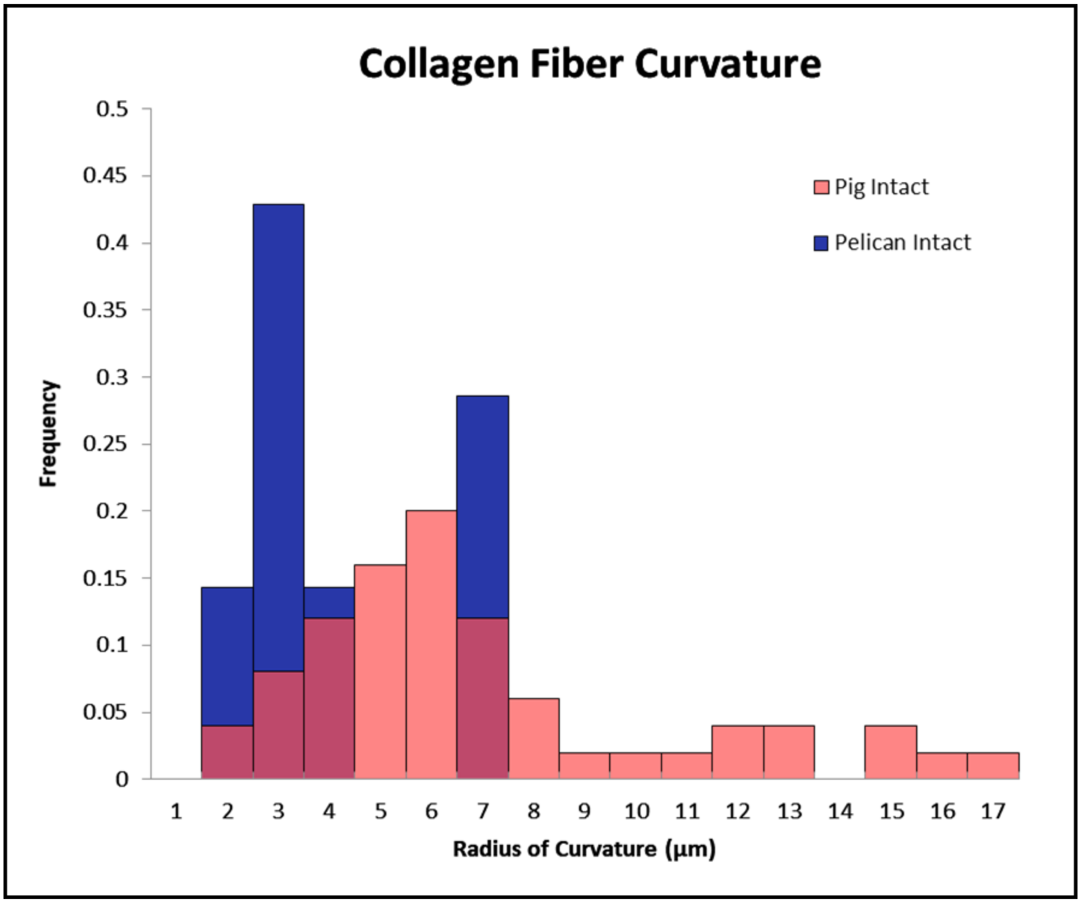

Figure 19: Comparison of pig [9] (top) and pelican (lower) radii of collagen fibers.

3.2 Age and Anisotropy

The two layers observed in the gular sac present are revisited in Figure 20. While the first two magnified images solely reveal a corrugated geometry, created by folding of the exposed surfaces, a seamline appears to exist in the lower left image. This transverse specimen snapshot is redrawn in the bottom right image in order to assist with locating the aforementioned seamline. Unfortunately, this particular specimen was of younger age, such that the dark coloration of grooving observed in adult birds has not yet been attained. Terming one bump of the corrugation as a 'tooth', Figure 21 was created after recording the tooth shape's deformation in the transverse orientation. The green curves represent the dark groove coloration areas on an adult specimen's gular sac and the red curve segments represent the sac segments connecting them. The illustration’s colors are solely for the tracking of groove pigmentation; they do not imply separate material compositions. The figure then illustrates how the corrugated structure must shift, align, and stretch in response to the depicted loading. Pockets begin to drop vertically while wall sections are drawn down and out, elongating the base level of the skin. The horns appear to be the last section of grooving to flatten—at this point, the tooth shape is reduced to miniature twin peaks. This process suggests that a second crimped structure may also contribute to the high extensibilities seen. Once the horns are pulled flush to the surface, the skin’s response relies on the behaviour of the microstructure. Fibers then proceed to realign and rotate, stiffening the skin until fracturing. The initial process (the first three images at the top of Figure 21), was not observed during tensile experimentation of longitudinal specimens. Since the grooving of the sac material aligned with the direction of applied stress, this preliminary sequence of events is does not occur. Longitudinal specimens simply stiffen until fracture, involving less microstructure rearrangement than transverse specimens. Future work with mature carcasses could provide additional data with respect to how groove dimensions change throughout the testing process, allowing the tracking of the accordion structure’s morphology.

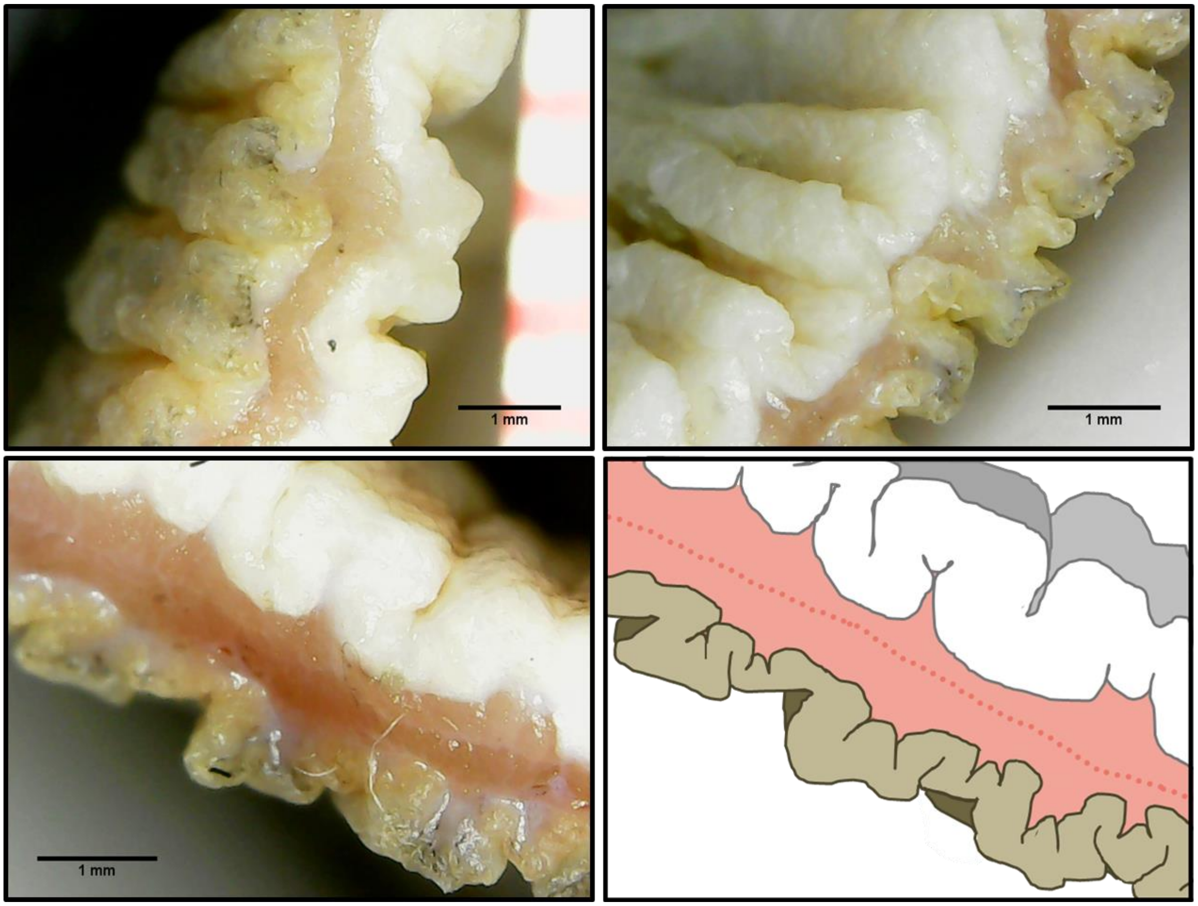

Figure 20: Magnification of the corrugated groove structure and splitting of the two layers of skin.

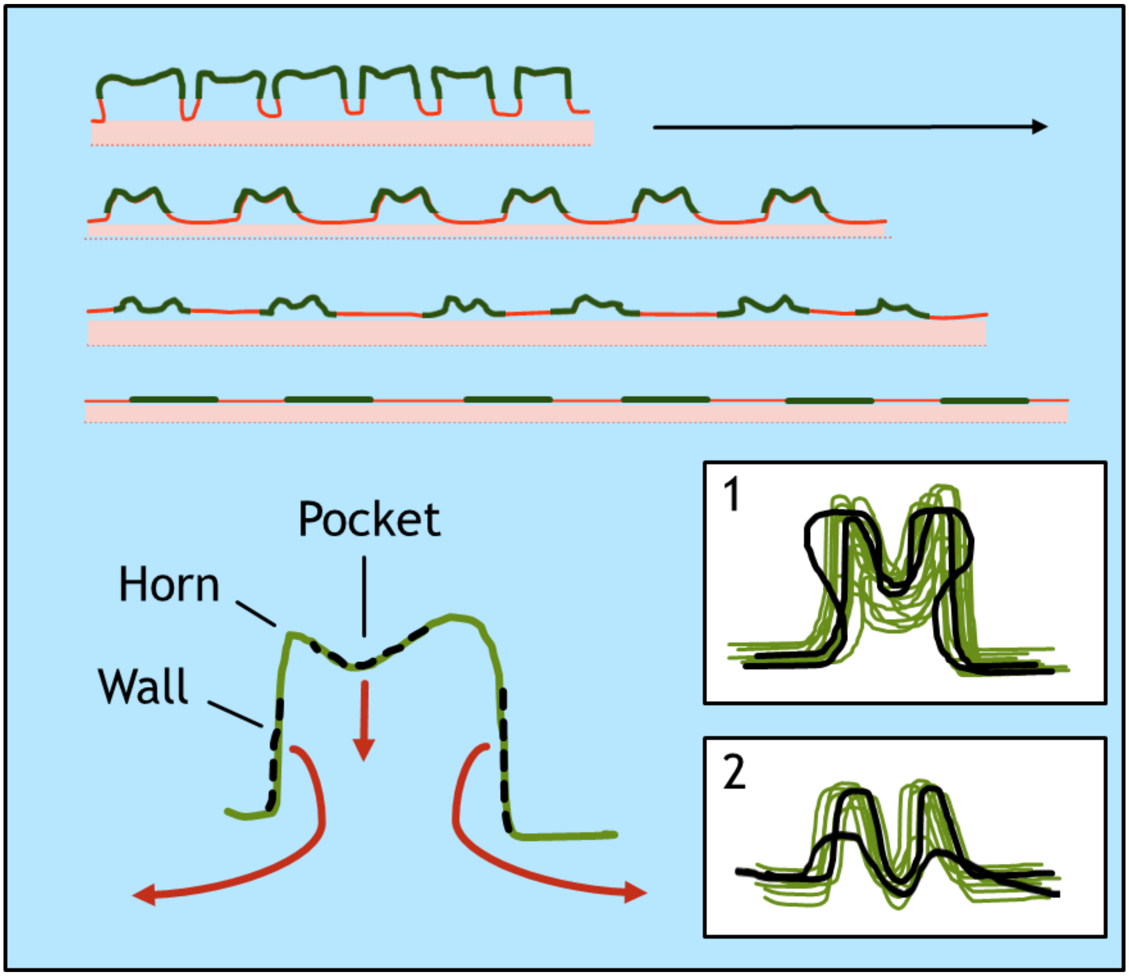

Figure 21: Diagram of the corrugated groove structure of the gular sac and how the cross-section of the sac deforms as it expands in the transverse direction. Dashed line segments indicate regions observed to move as segments during extension until the material is stretched to a flat state. Red and green image colorations signify difference in the pigmentation of the skin; it is not implied that these are distinct and separate materials.

Table 2: Description of all pelicans involved in this study. Blue rows indicate maturity.

Sample	Relative Age	Purpose
Pelican 1	Mature Adult (>3 years)	Strain Rate, Proximal, Age Effect, TEM
Pelican 2	Infant (<1 year)	Proximal, Dorsoventral, Age Effect
Pelican 3	Infant (<1 year)	Stress Relaxation (Not Discussed)
Pelican 4	Adolescent (1-3 years)	Dorsoventral, Age Effect
Pelican 5	New Adult (~3 years)	Dorsoventral, Age Effect
Pelican 6	Adolescent (1-3 years)	TEM, HR-SEM of fracture surface.
Pelican 7	Adolescent (1-3 years)	Microscopic images of corrugation structure.

Table 2 documents the relative ages of each bird involved in this study. A representative J-curve was created for each the four pelicans tagged with 'age effect' in the table. Figure 22 depicts these for each orientation in the hope that an obvious trend would arise. Curves were developed using the average and weighted average values of all extracted attributes located in Table 3. This table is organized with columns contrasting the property values as a factor of age. It is also separated by testing orientation in order to better isolate the effect of age. Figure 23 defines the experimental descriptors of the skin's response— reported on in Table 3. Each bird's respective values were plotted with the goal of correlating relative age to a consistent shift in material properties. Weighting the dataset minimally shifted curves, but did not improve the significance or even establish the pattern desired. Both orientations of specimens did not show the expected grouping. Rather than seeing separate sets of coincident curves and attributing this to difference in age, the data did not support such a distinction. It would be hard to group the curves by the observed age anyway because tensile responses were found to vary due to other factors like location in the pouch. The purpose of plotting these is to see if, at a simplified level, an obvious trend or grouping prevails. Absence of a pattern could additionally be explained by the inherent variability between individual birds. Brown Pelicans have been documented to live as long as 30 years so tagging a bird as simply ‘mature’ proves insufficient to characterize the age of the pelican from which the test specimens are derived. It is possible that age might be able to be separated into larger bins, such as five-year periods, so there would be clearer and more consistent evidence of property shift over life of the pelican. However, this approach was not feasible over the project timeline due to the difficulty of acquiring mature carcasses. SeaWorld was able to provide a number of infants, who failed to achieve self-sufficiency in feeding, but only a few of mature age. It is also far more challenging to distinguish an exact age for the birds inside the mature classification. Head plumage only provides a rough estimate (see Figure 3) and while this may be enough to establish categories of infancy and adolescence, it fails to partition the mature spectrum of carcasses received. Another possible explanation is that there is just no predictability to material properties using the age information of the pelican.

In addition to corresponding the plumage pattern to age, Figure 24 and Figure 25 plot the stress-strain data for mature and infant birds, respectively. Mature specimens produced curves that were quite distinct in separation, split based on the tested orientation. Longitudinal samples were associated with properties of high strength and low strain. Transverse specimens yielded at lower strengths, but for considerably higher strains. After addressing a few outliers, both mature plots exhibited nearly zero overlap in grouping established by testing orientation, as identified by little overlap of the transverse and longitudinal specimen responses. The first mature bird, tagged pelican 1, produced a data set consistent with anisotropy of the pouch material. Sampling of the second adult, labeled pelican 5, reveals property magnitudes quite different from those exhibited by the first pelican. Despite failing at, on average, half the other’s strength, these specimens were capable of handling larger strain before failure. This difference in behavior is attributed to the bird’s level of maturity. Assuming pelican 1 models the properties of a fully mature bird, pelican 5 is liable to belong near one of the boundaries of the adult spectrum— as either a newly grown or elder.

Immature specimens resulted in data sets showing varying degrees of overlap in the grouping of testing orientations. The first young bird, identified as pelican 2, generated tensile curves more closely resembling that of an isotropic material. The expected properties of each orientation were still evident in the distribution; longitudinal specimens fractured at higher strengths and transverse specimens endured larger strains. In contrast to the results for the mature birds, the responses of the specimens from the young birds have test orientation groupings almost completely overlapped, showing significantly less anisotropy than did the older bird’s pouches. Sampling of the second young bird, pelican 4, shows a distribution less isotropic than observed for pelican 2, but much more isotropic than the results obtained from the mature birds. While this bird is classified between the ages of infancy and adolescence, it was likely on the verge of becoming a fully-fledged adult—this is based off of how close the data looks to that of pelican 5. From these results, a bird’s age does not help distinguish which curve set is likely for an individual. However, these plots support the earlier musings of Field that age brings more distinct anisotropy in the gular skin [1].

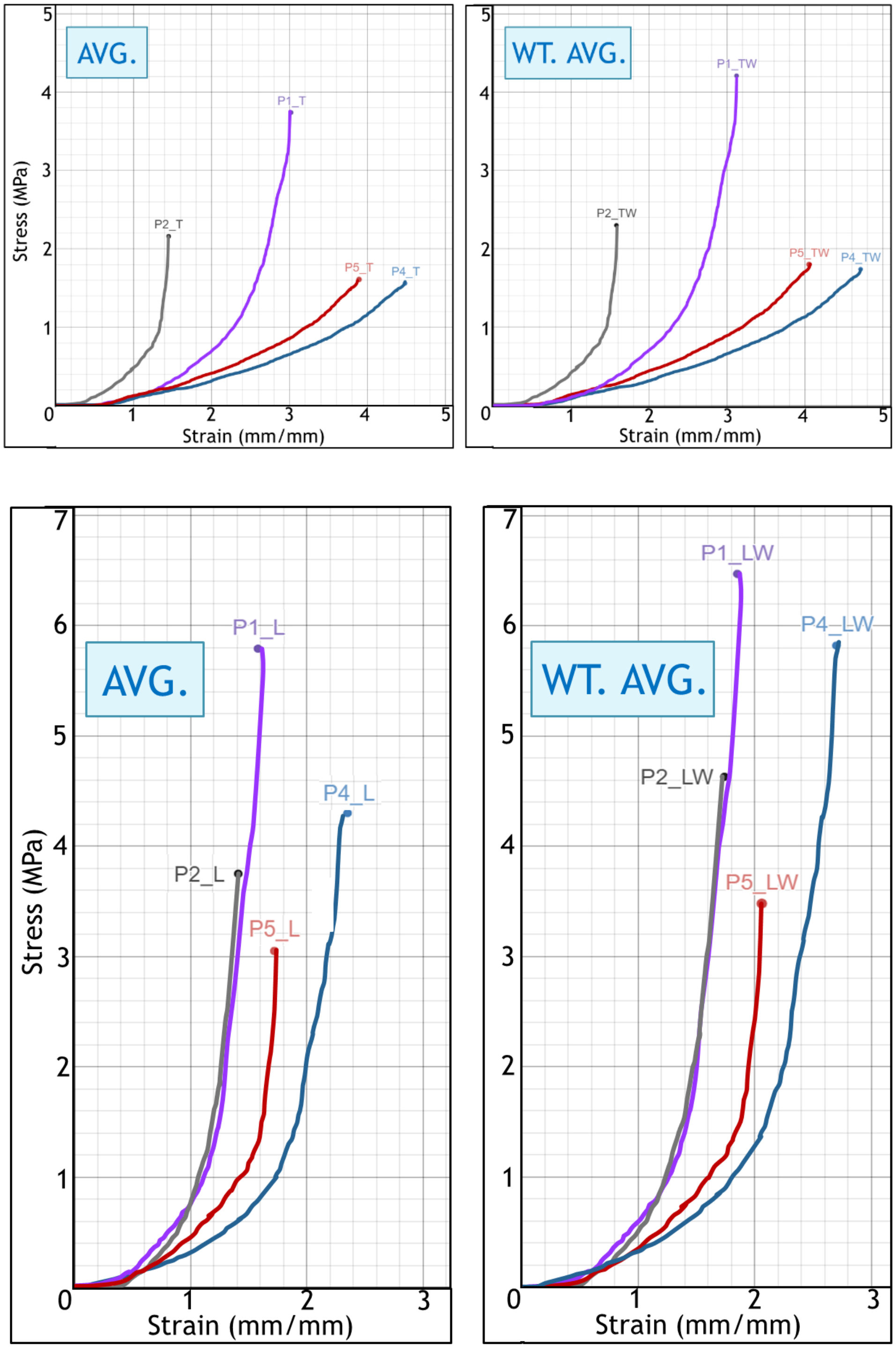

Figure 22: Comparison of pelicans 1, 2, 4, and 5 in representative parameters by orientation. Purple and maroon are older birds (>3 years). Black and navy blue are younger birds (~1 year).

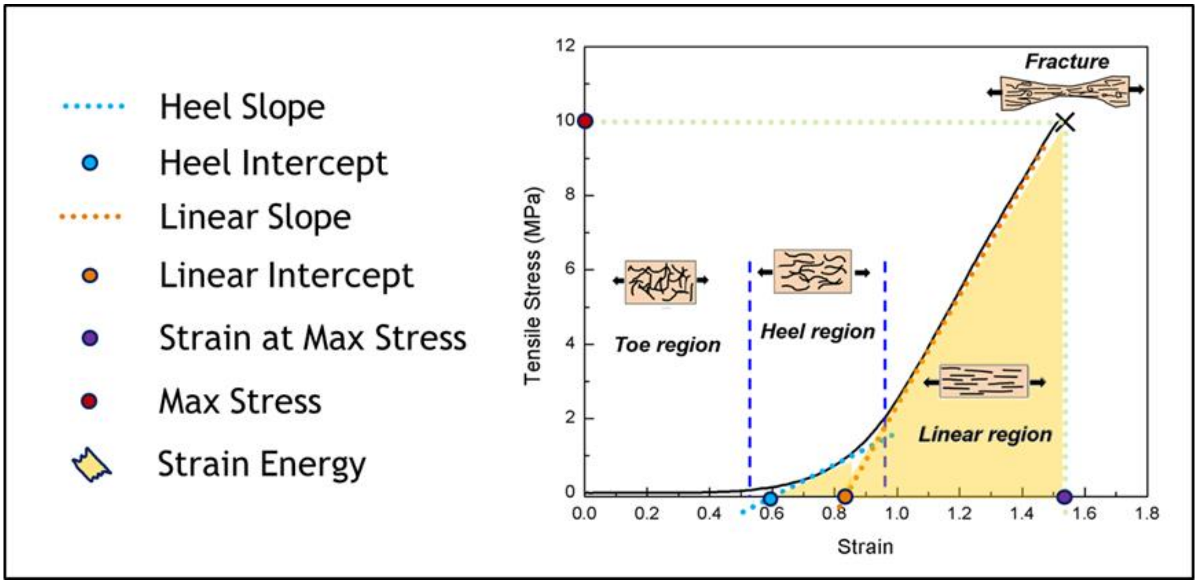

Figure 23: Description of regions in a typical skin response curve and depiction of fibril alignment during deformation. . Consider this a legend for Table 3, in which the following attributes are assigned values for each pelican.

Table 3: Comparison of the experimental values for pelicans 1, 2, 4, and 5. Note the red-green scale for max-min of parameters, respectively, as well as the age spectrum color scale.

	Orient.	Heel Slope [MPa]	Heel Int. [mm/mm]	Linear Slope [MPa]	Linear Int. [mm/mm]	Max Stress [MPa]	Max Strain [mm/mm]	Strain Energy [MPa/m³]
P2	Avg. Long	2.83	0.31	6.69	0.50	3.75	1.41	1.92
P4		2.43	0.57	4.96	0.84	4.30	2.35	3.09
P5		2.52	0.32	3.88	0.52	3.05	1.72	2.03
P1		4.97	0.43	9.36	0.56	5.79	1.58	3.26
P2	Wt. Long	4.45	0.38	9.36	0.59	4.63	1.74	2.60
P4		4.54	0.69	8.52	1.03	5.82	2.70	3.40
P5		3.81	0.44	5.48	0.74	3.48	2.06	2.22
P1		6.97	0.53	12.91	0.67	6.47	1.85	3.96
P2	Avg. Trans	1.68	0.42	3.71	0.69	2.16	1.45	1.03
P4		0.34	1.83	1.10	2.70	1.56	4.48	1.55
P5		0.50	1.98	1.46	2.52	1.61	3.89	1.22
P1		1.20	1.20	3.45	1.74	3.74	3.02	2.97
P2	Wt. Trans	2.21	0.51	4.31	0.86	2.30	1.58	1.12
P4		0.43	1.98	1.59	2.82	1.74	4.71	1.62
P5		0.65	2.08	2.19	2.67	1.80	4.05	1.27
P1		1.34	1.30	3.74	1.82	4.21	3.12	3.79

MAX
MIN

OLD
YOUNG

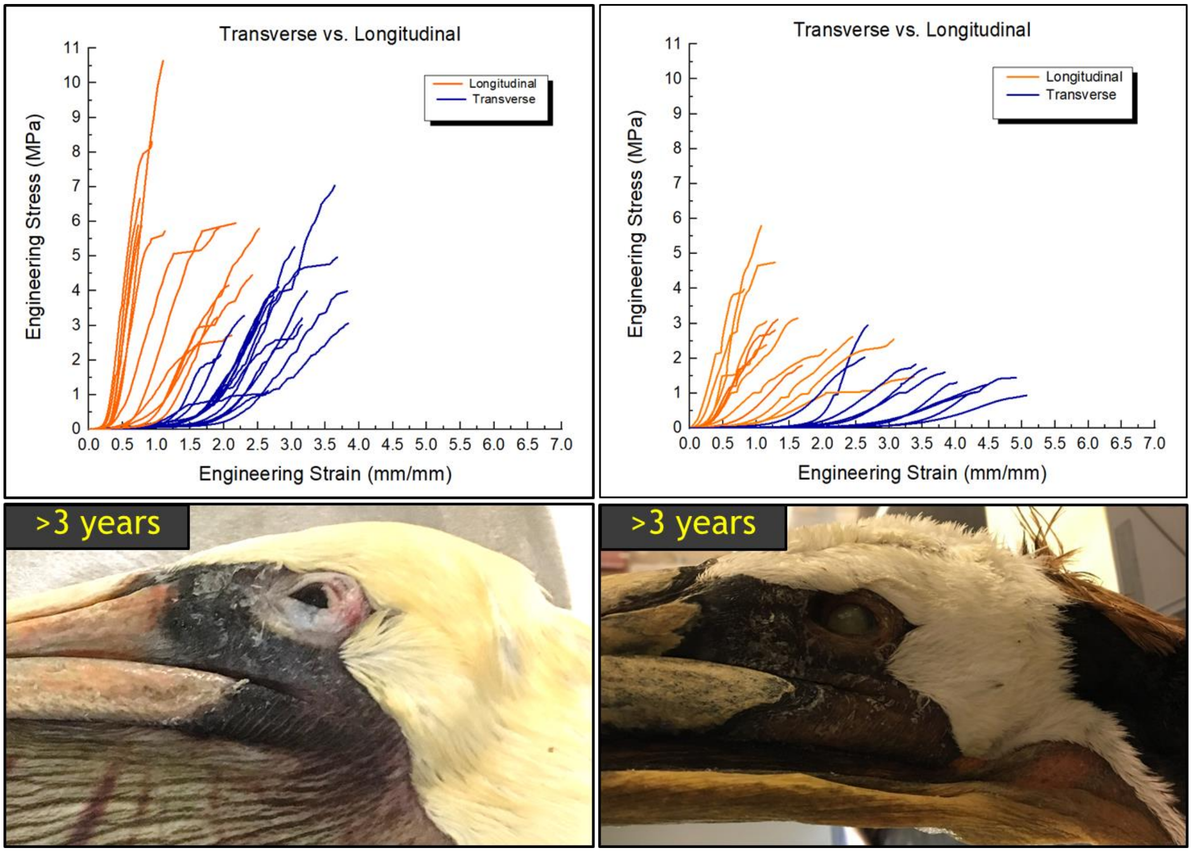

Figure 24: Comparison of pelicans 1 and 5 in terms of sample orientation. Note the anisotropy in the stress-strain curves.

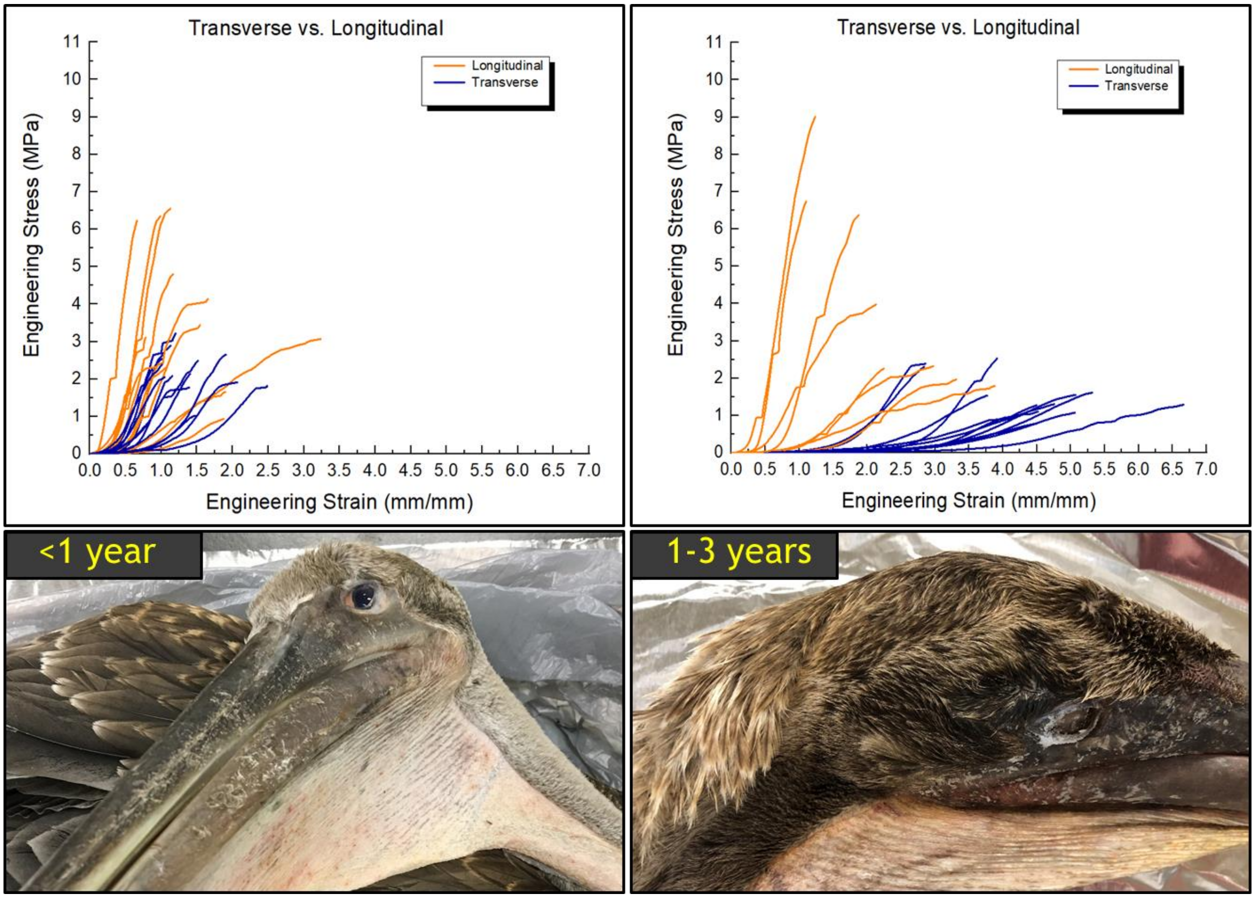

Figure 25: Comparison of pelicans 2 and 4 in terms of sample orientation.

The fourth and fifth pelicans were tested almost identically, with longitudinal and transverse assignments consistent in location between them. Since the fourth is a younger bird, tagged as one to three years old, and the fifth is an older bird, tagged as more than 3 years old, the effect of age should be a more isolated parameter.

Figure 26 and Figure 27 show the specimen orientations for pelicans 4 and 5. Figure 26 depicts the pouch of pelican between stages of infancy and adolescence. Figure 27, on the contrary, shows a mature adult pouch, one well over 3 years in age. Note that both sample maps are shown here to convey the consistency in the orientation and regional assignments applied. This allowed for the most precise comparison of a specimen's performance with a known difference in age.

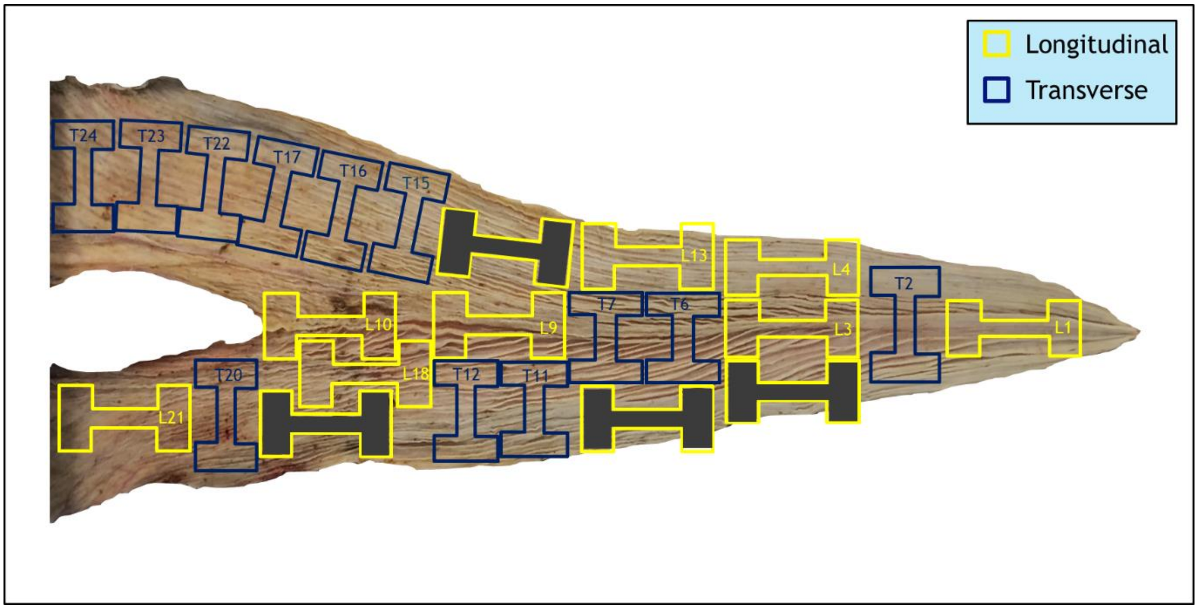

Figure 26: Adolescent (one to three years old) pelican 4's map of sample orientation.

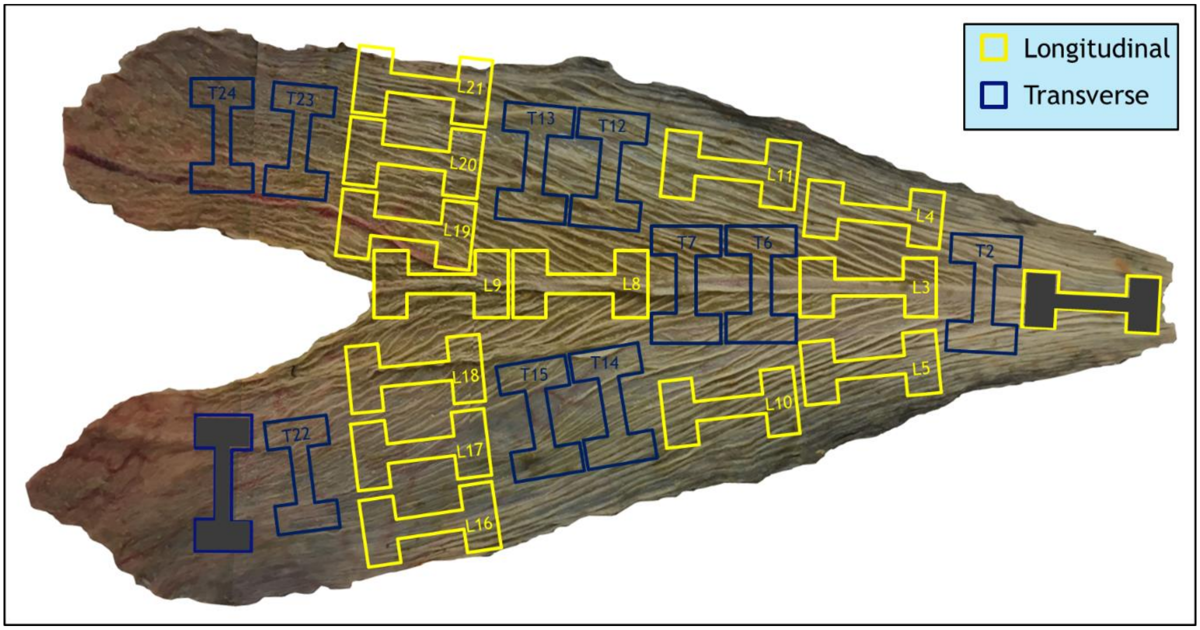

Figure 27: Adult (more than 3 years old) pelican 5's map of sample orientation.

3.3 Constant strain rate

A limited study assessing the influence of strain rate on the material properties was performed using the pelican 1. Note that ‘constant strain rate’ here actually means applying a constant displacement rate, and also keeping the loading speed constant during testing of a single sample. Experimental parameters defining the heel, linear, and failure regions were extracted from tests at standard strain rates of 10^{-3}, 10^{-2}, and 10^{-1} s^{-1}. Figure 28 offers several examples of these experimental attributes. Error bars in these histograms are far from reasonable; this results from a lack of data and great diversity between the few samples that represent each rate. Figure 29 displays the array of stress-strain curves. Note that each orientation only includes a single sample at the slowest rate and several at the sped up loading. In the plot, tensile curves cluster in groups containing dissimilar strain rates so it is difficult to derive any sort of meaning from this representation—even with data split by sample orientation. The histograms, while not a good model of the rate’s behavior, indicate a larger effect via the longitudinal orientation. Strength characteristics reported in the figures were derived from linear fits of slopes measured in each respective region. For the heel regime, longitudinally oriented samples increased in strength with increasing strain rate. Transverse samples behaved independently of strain rate. Within the linear region, both orientations increased in strength with increasing strain rate, but to a larger extent for longitudinal.

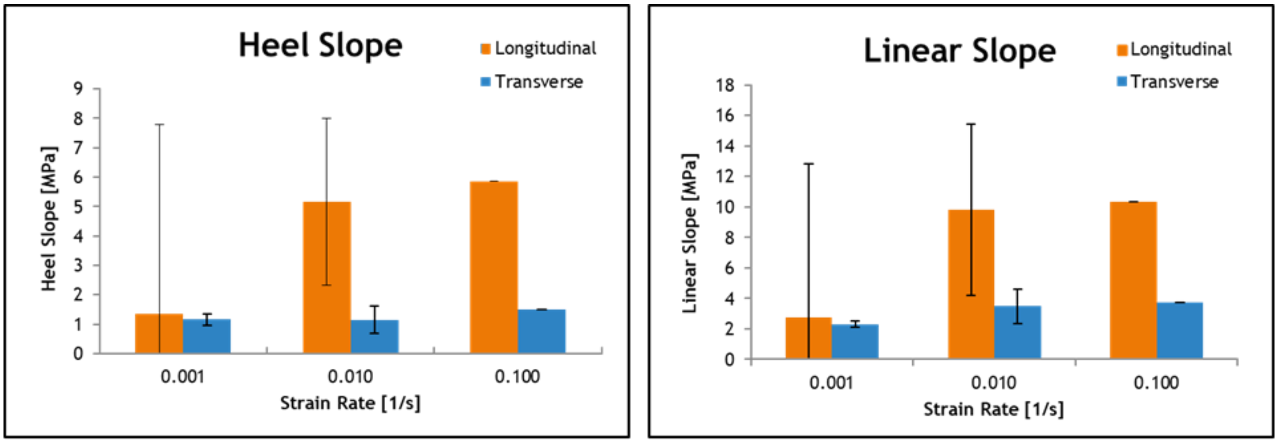

Figure 28: Distribution of heel and linear region attributes by constant strain rate for Pelican 1.

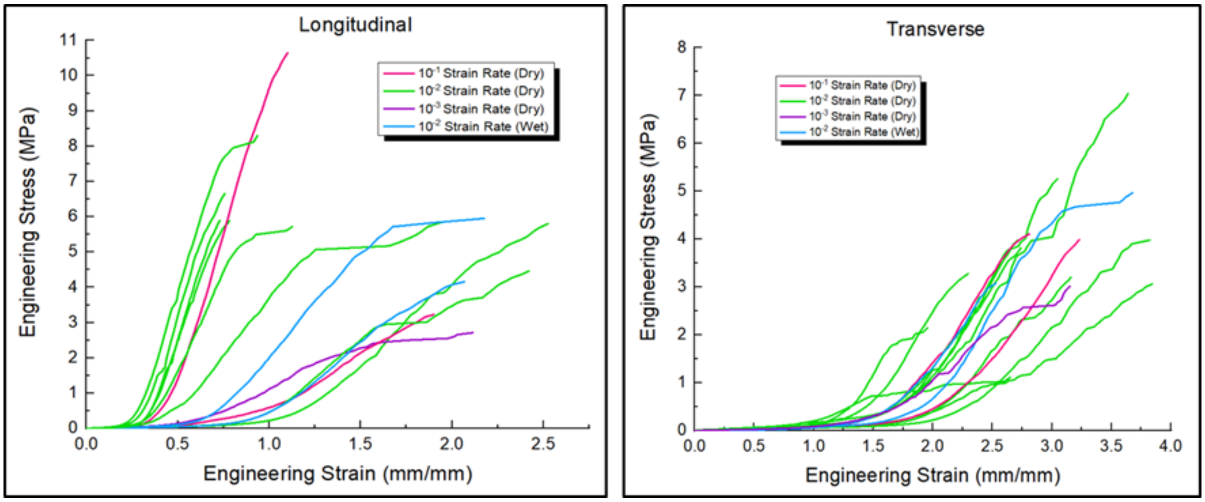

Figure 29: Pelican 1's average tensile curves for strain rates spanning two orders of magnitude.

Curves produced using 10^{-1} and 10^{-3} s^{-1} strain rates were analyzed alongside those done for rabbit skin under similar loading conditions [8]. Figure 30 and Figure 31 align the horizontal axes, allowing for more direct comparison of engineering strain between the two sets of results. Neither the maximum stresses nor the strains are very similar. The pelican's curves yielded failure stresses consistently less than those exhibited by the rabbit skin. The pelican's strains at failure, however, were measured to be much greater than those reported for the rabbit skin. Examining the transverse plot, curves appear to only just begin at a strain of 1. It may seem that the data should be shifted to the left to with the effect of reducing the strains at failure. However, since not every sample shows evidence of this behavior, this action was not performed. This behavior would seem to be explained by the unfolding of the skin in the transverse direction as shown in Figure 21. This unfolding or flattening of the skin during transverse loading would be expected to have large strains with little load until the corrugated cross-section is flattened. Knowledge of rorqual whale VGB further supports the unusual results seen in Figure 31. VGB tissue has been reported to extend up to 400% its original length in the circumferential direction [6]. Furthermore, the material does not begin to climb the J-curve shape until strains of 1.

Figure 32 compares maximum stress and strain results for tensile tests at different rates for the pelican and pig data. At the failure point, the maximum obtainable stress was generally higher for faster loading rates. The failure strain measured in each test was essentially independent of strain rate. Despite the dataset only containing a few specimens loaded at 10^{-3} and 10^{-1} s^{-1}, all trends observed across the select strain rate trio were consistent between pig and pelican. However, the pig data maximum stress values are more similar to those observed for rabbit than for pelican, with failure stresses for pig and rabbit from 2-4 times greater than the values for pelican. There also appears to be a greater disparity between maximum strains by testing orientation in the pelican compared to the pig. The higher maximum strains in the transverse direction, for the pelican, are one indicator that the pelican gular sac is more extensible than the skin of the other two animals.

In summary, curves possessing unusually high failure strains were observed for about half of the dataset for the elder bird. The rest of the dataset includes curves that have strain values more comparable to those of rabbit and pig. The appearance of two distinct curve groups was most prevalent in mature pelicans. Since these strain-at-failure groupings aligned with specimen orientation, there is substantial evidence supporting the material’s increasing anisotropy with age. All samples underwent identical testing environments and post-processing for smoothing minor slippage before and during the sample’s stretch. No bias was practiced during testing or the analysis that followed.

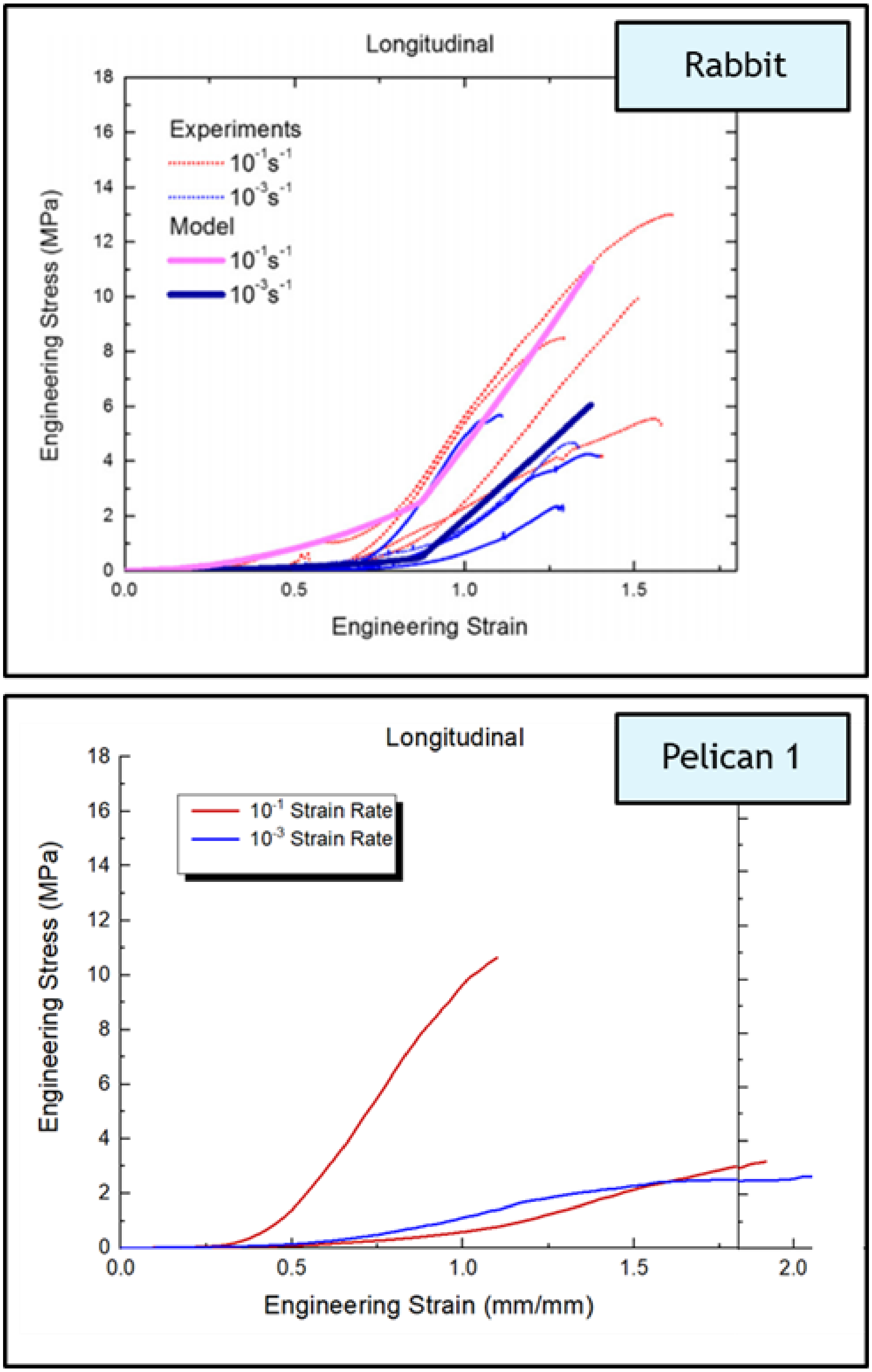

Figure 30: Comparison of longitudinal specimens of rabbit skin and pelican gular skin at strain rates of 10^{-1} and 10^{-3}. Rabbit data from [8]. Top figure rabbit, lower figure pelican.

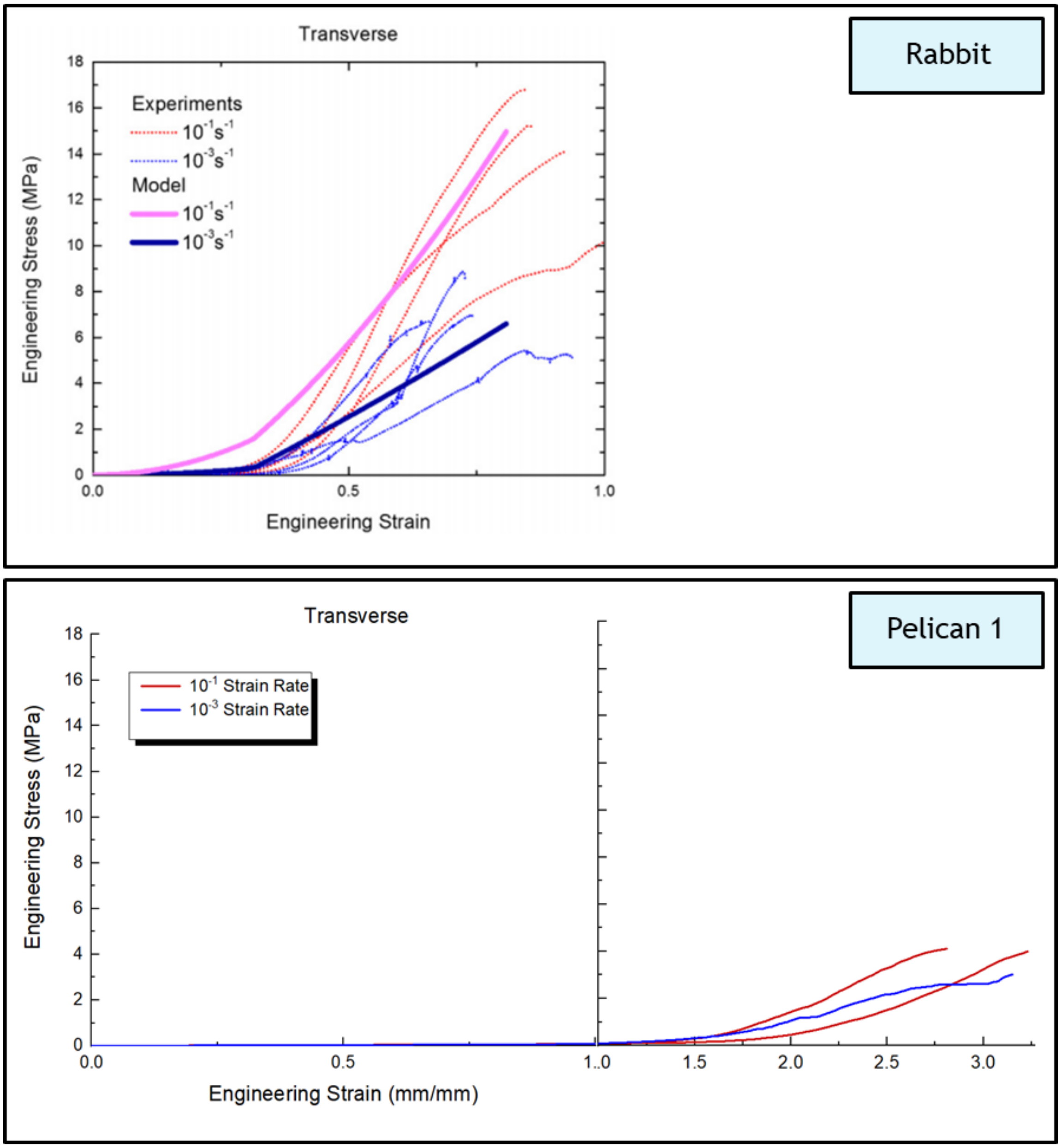

Figure 31: Comparison of transverse specimens of rabbit skin and pelican gular skin at strain rates of 10^{-1} and 10^{-3}. Rabbit data from [8]. Top figure rabbit, lower figure pelican

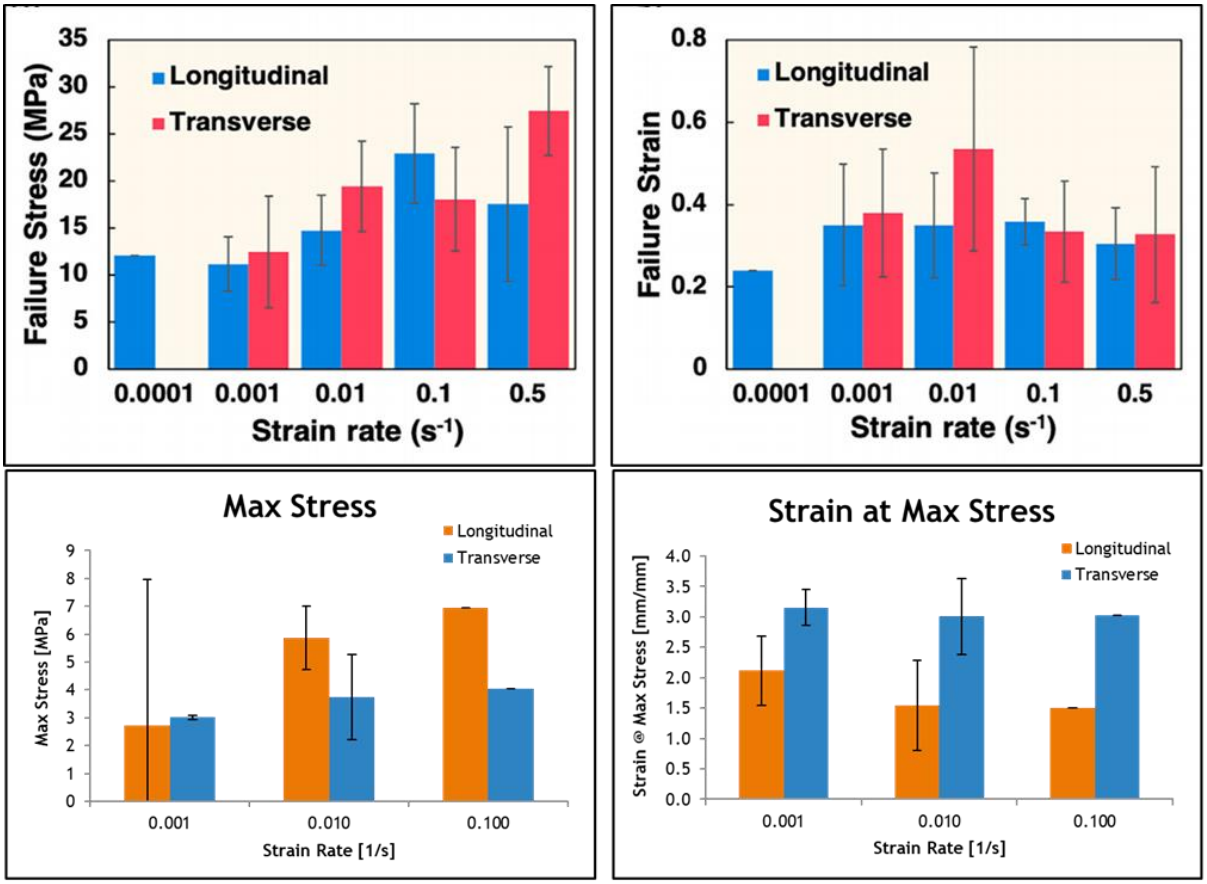

Figure 32: Comparison of pig and pelican maximum stress and strain at failure [9].

3.4 *Property variance by location*

Since the gular sac tissue yielded an assortment of values for each location and testing parameter, an attempt was made to isolate which sort of directional variation was most influential to the properties of the material. Figure 7 illustrates the terminology behind directions evaluated for potential variation; anteroposterior and dorsoventral. The dorsoventral direction is from the mandible to the belly of the pouch. The anteroposterior direction is along the beak, from its anchor point in the skull to the tip. This will be referred to as the proximal direction for all further discussion.

3.4.1 Proximal variation

Overall, the experimental values appeared to fluctuate little across partitioned regions targeting proximal variation. Figure 33 displays an example of one parameter's histogram. Transverse orientated specimens produced a maximum stress that was consistent over the pouch partitions. Longitudinal orientations did show a bit more variability, however, there were no distinguishable trends, either towards the skull or the beak tip. The outer regions, labeled here as 4 and 6 in Figure 33, were found to yield similar responses, while the inner partition was observed to be either higher or lower than the outer regions. It's possible that the partitions created were too large such that variation between regions was not significant and that observable patterns were consumed as variation within in a region. Therefore, study of this direction of variation continued with later pelicans in the hope that a second pelican, with more refined partitions along the pouch, would show more observable trends of the skin properties with location.

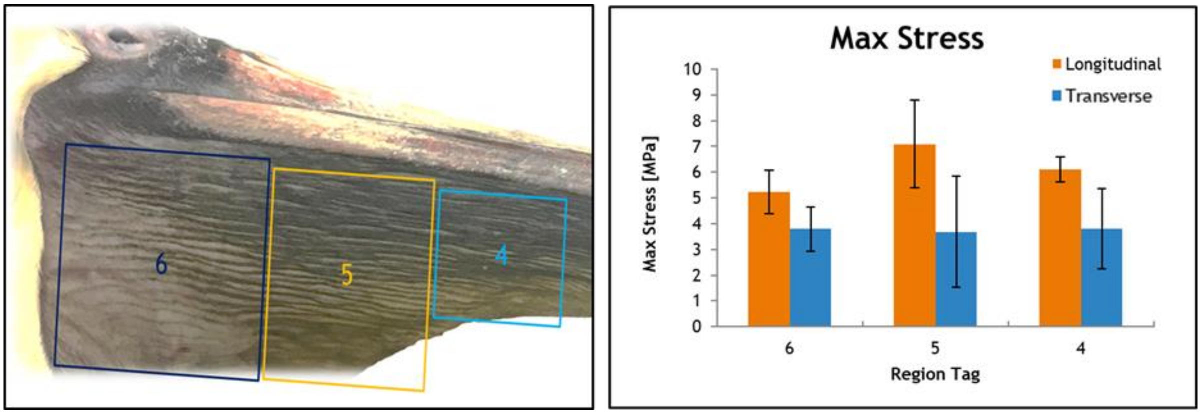

Figure 33: Pelican 1's proximal study with heel region attributes and strain energy.

The next bird's sample space was partitioned in a somewhat more refined manner, with division of the pouch's full length into 4 distinct proximal sections. Figure 34 labels the regions 4 to 1, decreasing in number towards the beak tip. The histograms for this pelican include an extra partition relative to pelican 1, but the transverse specimen for partition 1 did not yield usable results due to excessive slippage.

This data suggests transverse specimens are capable of handling higher stresses in regions closer to the skull. Note that this trend consists of three regions because the pouch space near the beak tip allowed for only a few samples. Longitudinal orientations did not indicate any sort of trend. Consistently seen with all measured responses, the results are as follows: outer regions response levels were observed to be fairly consistent while inner regions did not have a consistent trend, found to be either higher or lower than the values for the outer locations. Trend expectations were of the steady increase or decrease of properties; this could have been correlated with observations of leaner skin near the skull and thicker skin by the beak tip.

Figure 35 identifies curves with their respective location for each specimen orientation. In short, the results for longitudinally oriented specimens did not show clear evidence of any trend. Curves were generally similar to others from the same region, however, the relationship between these groupings didn't indicate any significant meaning. The inner partitions, which might be expected to have very similar values for the mechanical property metrics, were actually the most variable. Region 3 failed at higher strengths while region 2 broke at high strains and low strengths.

The transverse plot did show tighter grouping for the anchor locality, region 4, but displayed more variability for the majority of partitions. The transverse curves confirm the information observed in the previously discussed histogram of Figure 33, where it was evident that properties trend along the proximal direction. Note, however, that the pouch was only divided into three sections for that dataset. Visualization of the data using the histograms and the stress-strain curves both suggest the following trends from skull to beak tip: decrease in maximum stress, increase in failure strain, and decrease of the elastic modulus for heel and linear regions of the stress-strain curves.

Why might the properties trend this way? The skin near the beak tip can unfold much more than at the skull. This might allowing higher extension and therefore strain, but the skin is thicker at this location so should be able to carry more loading than the fragile skin attached at the skull. The stiffness trend seems reasonable because the skull region skin is already thin and the most ‘pre-stretched’. This skin would likely break at relatively low strains rather than undergoing the various collagen straightening behavior that delays failure and allows for high strains to be reached.

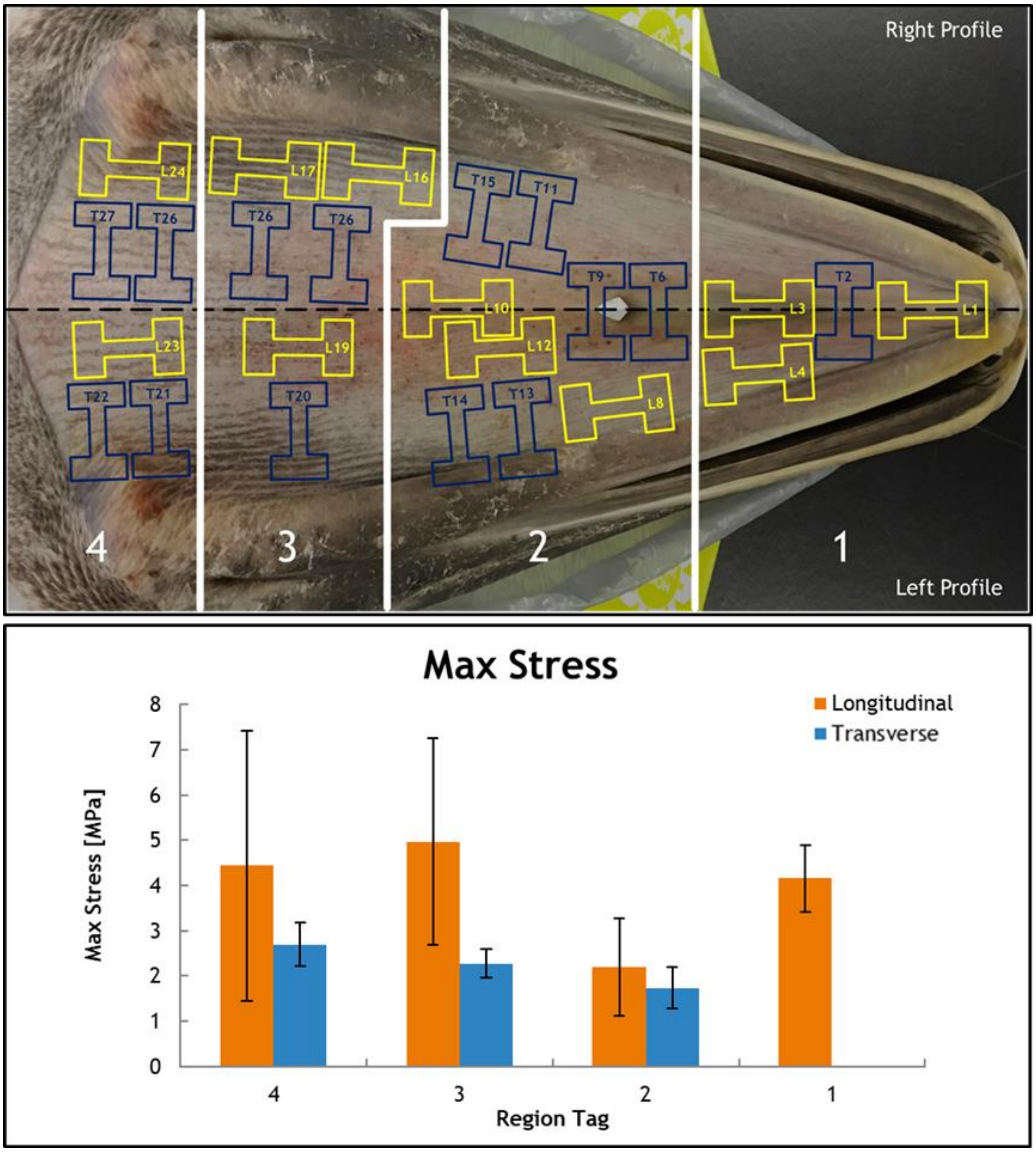

Figure 34: Pelican 2's distribution for proximal variation.

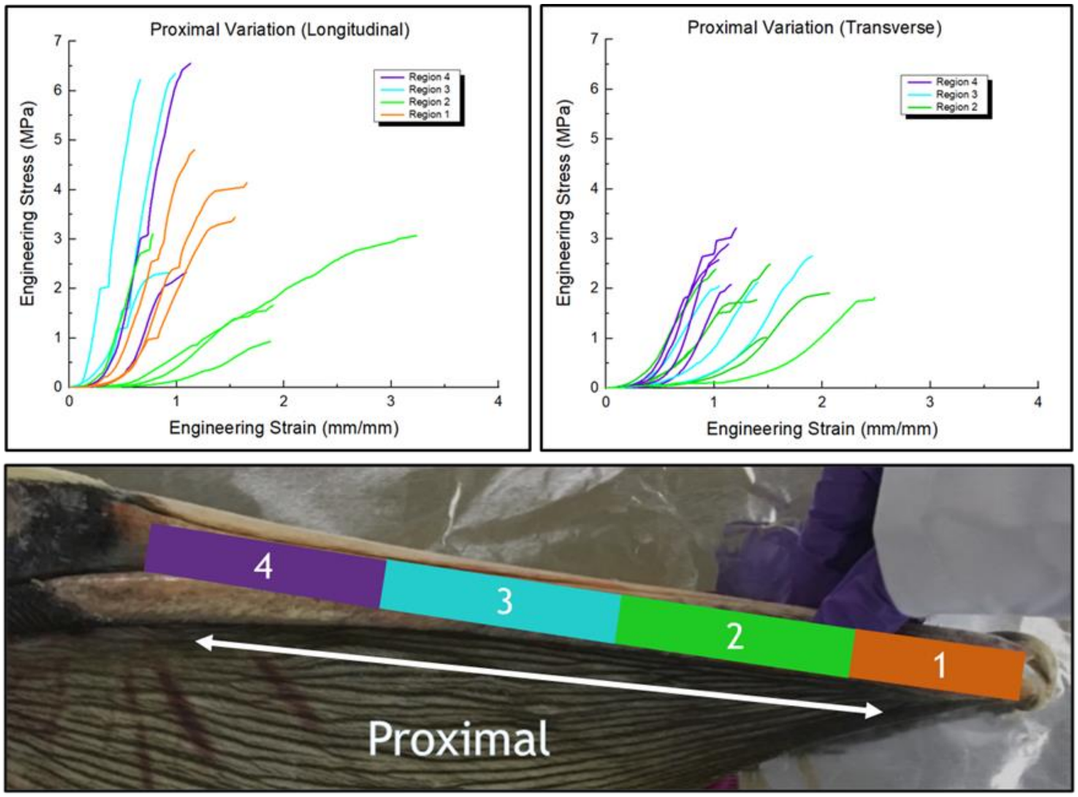

Figure 35: Pelican 2's results for proximal variation in longitudinal and transverse orientations. Region tagging for legends of the attached plots.

3.4.2 Dorsoventral variation

Sample spaces were 'heat-mapped' by intensity of property values in order to track variation across the pouch and possibly correlate these trends to observations of the material at these locations. The specimen's coordinates along the anteroposterior axis have already affirmed themselves as a minor influence on the properties exhibited, however, the color maps do not quite mimic the patterns observed in this study. This suggests that the alternative direction, or dorsoventral axis, may also influence how a specimen performs to an equal or greater extent. Figure 36 and Figure 37 display the regional classifications for samples involved in the study of this variation. Dog-bones specimens that were in approximately the same location of each pouch received the same testing orientation and dorsoventral region designations. This was particularly useful for interpreting anomalies in the plots of stress-strain curves.

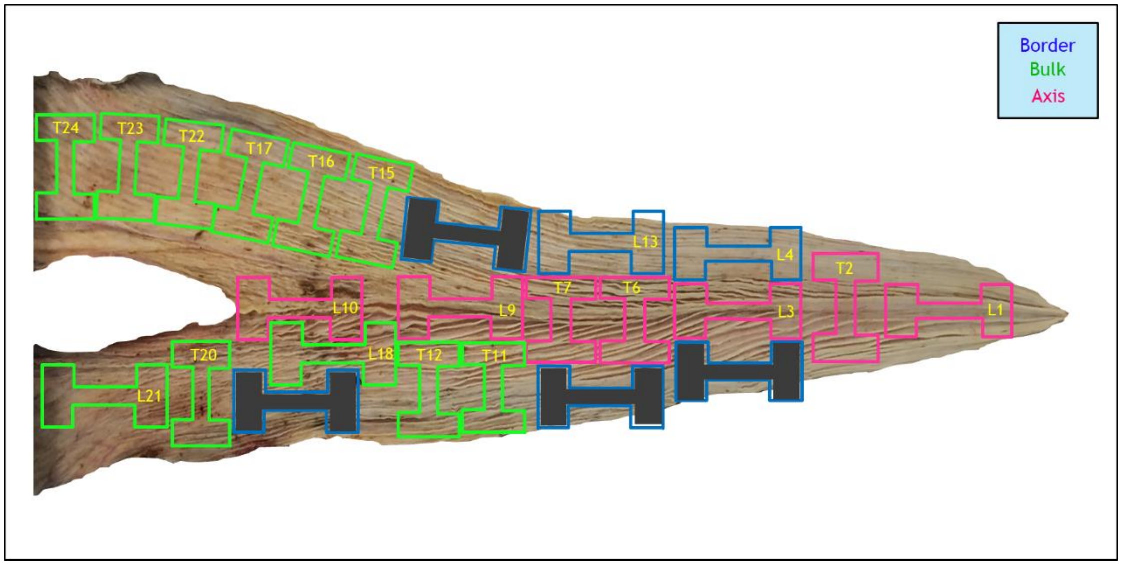

Figure 36: Pelican 4’s map of region tagging for dorsoventral variation.

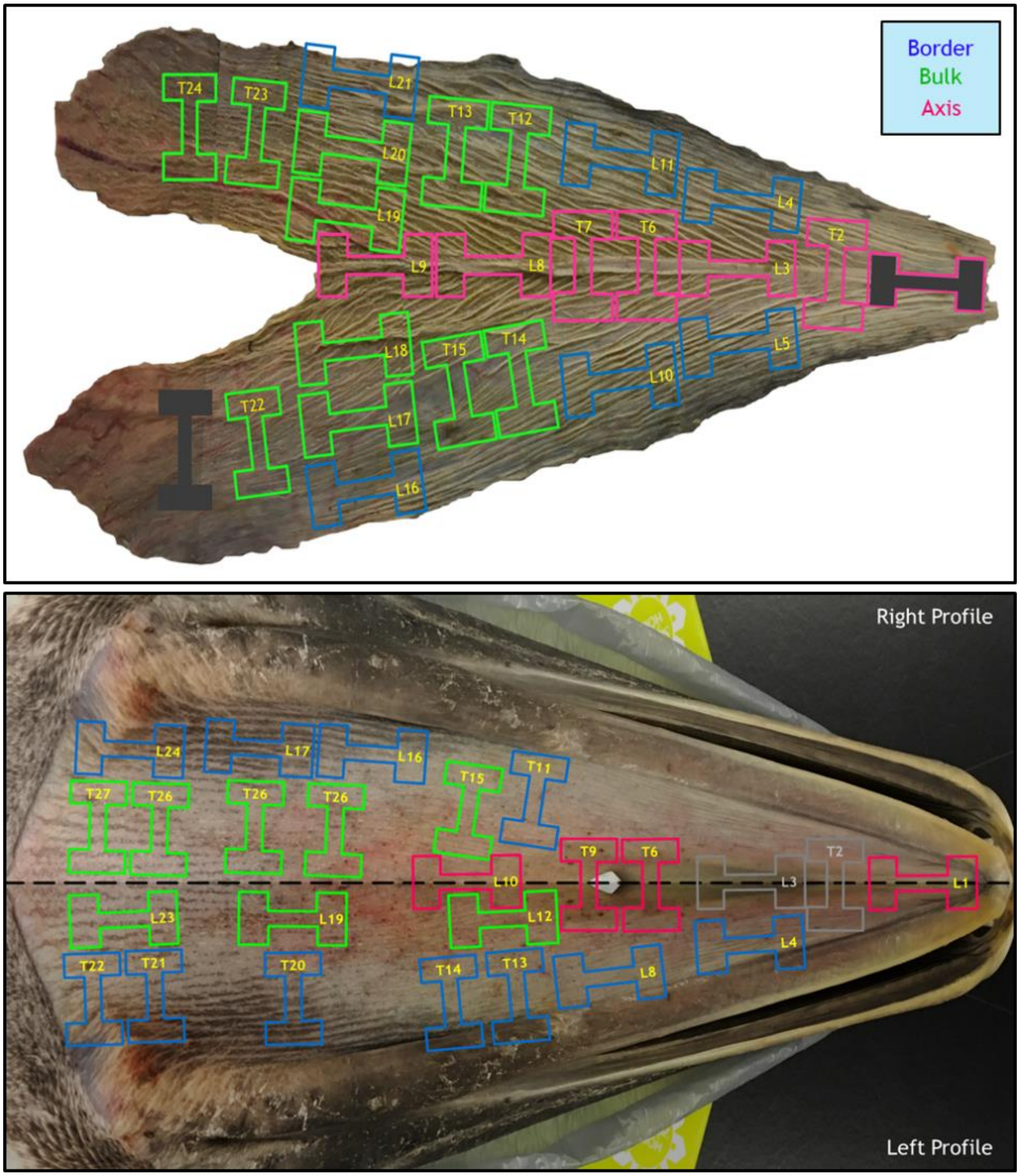

Figure 37: Pelican 2 and 5's maps of region tagging for dorsoventral variation.

See Figure 38 and Figure 39 for the results of pelicans 2, 4, and 5 for transverse and longitudinal orientations, respectively. The mention of an anomaly alludes to the fuchsia-colored 'axis' transverse curve with the lowest strain, in subplots b and c of Figure 38. This specimen, recorded as T2, was produced from the section nearest the beak tip, where the pouch narrows to a point. Since this location technically falls under both ‘axis’ and ‘border’ areas, the sample should exhibit property values between those measured for those two locations. Subplot (d) of Figure 38 provides the location of the ‘border’ grouping; curves for this region show specimens of moderate strength, but consistently fail at the lowest strains. All subplots support the ‘axis’ category as an extensible, but low strength region. As expected, the specimen incorporates attributes from each of the regions it neighbors.

Specifically, T2 demonstrates elevated strength, associated with ‘border’ samples, and handles substantial strains, typical of ‘axis’ samples. The geometric limitations of the pouch space meant samples often belonged to multiple dorsoventral regions. This offers an explanation for the shifted appearance of curves from this area and for the widespread variation in a single region’s dataset.

‘Bulk’ samples generally produced curves between those tested as a ‘border’ or ‘axis’. Fluctuation within this category was dependent on which auxiliary region a specimen fell nearest.

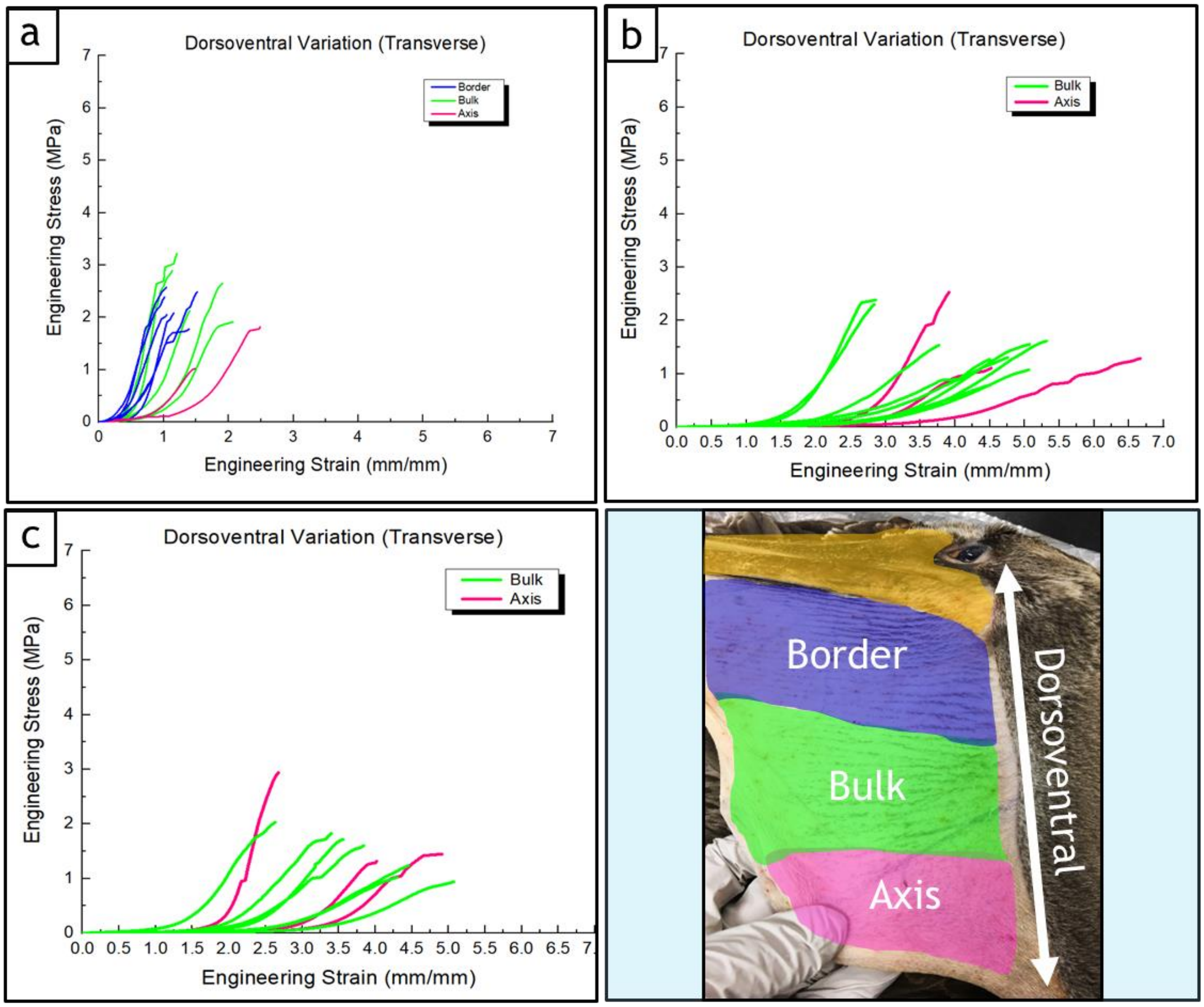

Figure 38: Comparison of pelicans 2 (a), 4 (b), and 5 (c) for dorsoventral variation in the transverse orientation , shown respectively in order of top left, top right, bottom left.

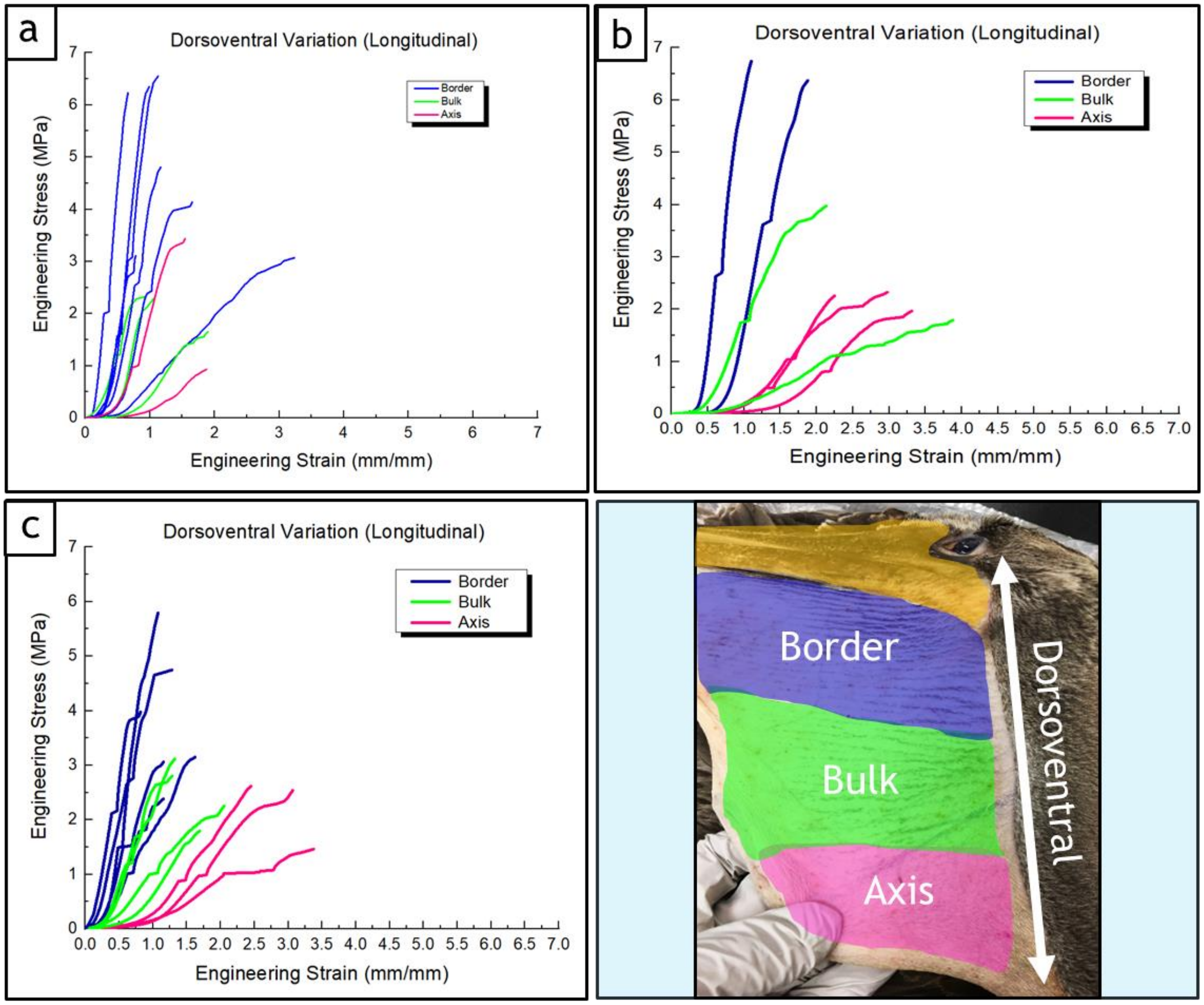

Figure 39: Comparison of pelicans 2 (a), 4 (b), and 5 (c) for dorsoventral variation in the longitudinal orientation , shown respectively in order of top left, top right, bottom left.

Trends observed in the transverse array of plots were even more apparent in the longitudinal. The second bird, subplot (a) of Figure 39, yielded curves displaying moderate grouping, but with considerable overlap in the partitioned regions. There are a few possible reasons for this, the first being the bird's relative age. This pelican, classified as an infant, possessed a pouch that behaved like an isotropic material. The majority of curves should overlap one another because this characteristic proved much more dominant an influence than variation across the proximal or dorsoventral directions. For the second justification, recall the remarks on dual-region assignments. The fuchsia-colored ‘axis’ curve most adjacent to the cluster of ‘border’ samples was of beak-tip location as well. Belonging to both regions, L1 manifests attributes of increased extensibility and strength, diverging from the typical groupings defined as ‘border’ and ‘axis’ regions. Subplot Figure 39 (b) also depicts the variability in material response of a younger bird, but the regions represented appear much more distinct. The anomaly of this set is the ‘bulk’ curve that transects the ‘axis’ cluster. Figure 36 actually shows L18 pressed up against the ‘axis’ L10. This pair of longitudinal samples nearly lay upon one another due to adjacency in both proximal and dorsoventral directions. It is less surprising then that this specimen does not group with the idealized ‘bulk’ responses. Subplot Figure 39 (c) displays the best array of results supporting the hypothesized variation. Since this source bird was of mature age, the spread adopts some degree of anisotropy—curves will tend to overlap less. The available pouch area was also more spacious, allowing for gaps between neighboring specimens. This meant regional classifications could be more clear-cut and specimens would behave as those in a single locale. The divergence in each dorsoventral region is much clearer than for the other birds.

Further evidence of these trends in material response with dorsoventral location is provided through the histograms of Figure 40, which display the data extracted from the stress-strain curves but quantified through averages and uncertainties of each property. Overall, all birds’ material characterization test data reflected the following trends in experimental attributes:

Longitudinally oriented samples clearly decreased in maximum stress and elastic moduli of heel and linear regions for the direction border-to-axis. On the contrary, these specimens showed increased failure strain and strain intercepts of the heel and linear regions for the direction border-to-axis.

Transversely oriented samples followed, in part, the longitudinal trends, increasing in failure strain and strain intercepts of the heel and linear regions in the same direction of travel along the dorsoventral path. These trend similarities could indicate regional variation independent of testing orientation. This would support the hypothesis that a specimen's dorsoventral location influences the properties associated with it.

'Border' region samples were determined to exhibit higher strengths while 'axis' samples displayed higher strains at failure. The pouch material, therefore, appears to display a gradient of tensile properties which vary along the dorsoventral axis.

The skin near the beak, in the 'border' region, must possess higher strength in order to maintain a tight connection to the hard beak. Consider the analogy of a fish dip net to the pelican's widespread open beak. Dip nets are swept through the water, frames enduring the hydrodynamic forces thrust upon them while retaining a sturdy inlet for maximum engulfment. How well the net is attached to the frame determines the success of the tool - a tear at the interface is much more likely to propagate than a tear in the bulk material. Typical net-frame design consists of a border of net material hoops, with the rings fully encircling the framing structure. This design doesn't work for the pelican because the upper mandible features relatively sharp edges which would cut through soft material present on the lower beak's upper surface (where upper and lower beaks meet). Even if the upper mandible enveloped the smooth, elliptical cross-section of the lower one so that the two parts of the beak did not meet face-to-face, the action of closing the beak with a wriggling fish or jostling a closed beak would produce friction, wearing away any non-bone material present for pouch attachment. The pouch material therefore 'clothespins' or grips the bone, becoming increasingly mineralized as it adheres along the lower mandible's exterior surface.

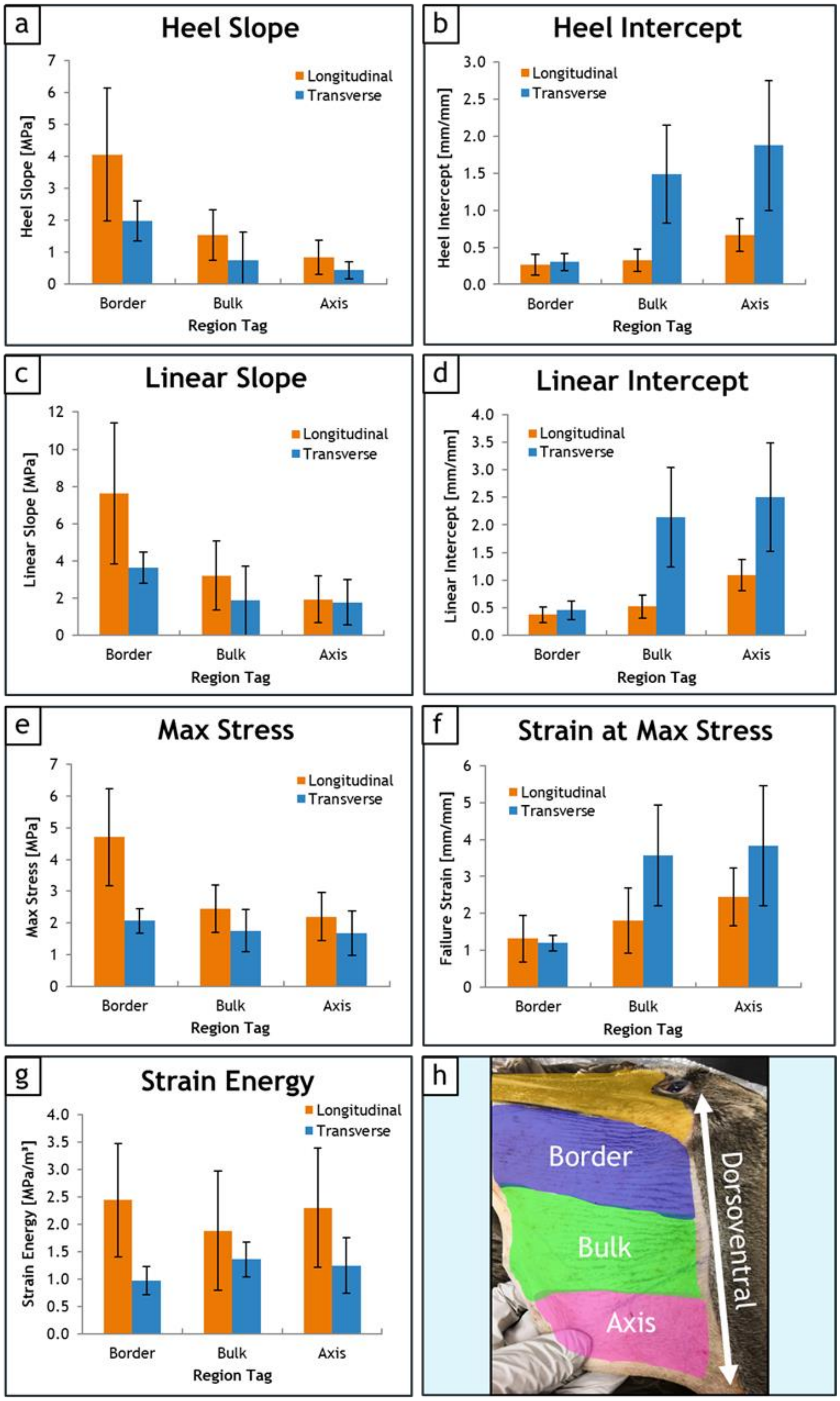

Figure 40: Comparison of dorsoventral regions for all experimental attributes in both orientations. Note that pelicans 2, 4, and 5 are binned together; age may be a cause for variation.

The skin belonging to the ‘border’ region possesses significant strength because it exists at the higher end of this hardening gradient, with the sole purpose of remaining attached to the more mineralized pouch rimming. Contrast this to the ‘axis’ region, which contains a thicker foundation of muscle tissue responsible for control of pouch inflation by pulling the pouch open as water presses into the pouch. Figure 41 shows the seam that runs the base of the pouch, a line of symmetry in the pouch. This may help the pouch relax in a more aerodynamic form and help maintain some of the initial shape during filling. This region is capable of higher extensibility, stretching its thicker dimensions further than the other defined regions.

Figure 41: The fifth pelican’s ‘axis’ region consists of a thicker line of collagen along the pouch base.

3.4.2.1 Statistical Analysis

The JMP statistical software package [14] was used to perform multiple regression analysis to assess the influence of sample orientation, location, and age (mapped by pelican sample) on the responses shown in Figure 40, namely heel slope, heel intercept, linear slope, linear intercept, maximum stress, strain at maximum stress, and strain energy.

In general, data from the skin tensile tests produced results with a large spread in measured parameters. This is not unusual for biological samples like these, but it does lead to very large uncertainty bars and makes inferences about the correlations between factors and parameters less certain.

Multiple analysis of variance data (MANOVA) results and scatter plots of the data are shown in Appendix A.

Table 4 provide results of a multiple regression analysis on the dorsoventral data, assessing the correlation of the parameters used to identify the specimens (orientation of the specimen on the pouch, location on the pouch, and estimated age on the response parameters.

The regression analysis was performed by first including all factors in the model. The largest P-value factor was then removed and another regression analysis was performed. This again was followed by removing the P-value with the highest parameter, just leaving a single factor (following [9]). All of the multiple regression models, even when just considering the main factor had P-values < 0.001. This main factor was most often specimen orientation, indicating a strong influence of the pouch material's anisotropic behaviour due in large part to the folds that run across the width of the pouch. Location, mainly by specimens on the border region of the pouch, was generally strongly correlated with the material response. Responses for specimens on the axis and bulk areas of the pouch were not statistically significantly different for the parameters considered.

Age was also was strongly correlated with parameters except for maximum stress and heel slope.

Table 4 highlights the model for each parameter with the largest adjusted R-square value.

Table 4: Multiple regression analysis of the influence of sample orientation, specimen location, and pelican age (estimated) on heel slope, heel intercept, linear slope, linear intercept, maximum stress, strain at maximum stress, strain energy.

Parameter	**P-value**				**Adjusted R-square**
	Model	Orientation	Location	Age	
Heel Slope	< 0.001	0.0017	< 0.001	0.849	0.522
	< 0.001	0.0014	< 0.001	*	0.535
	< 0.001	*	< 0.001	*	0.460
Heel Intercept	< 0.001	< 0.001	0.005	< 0.001	0.681
	< 0.001	< 0.001	*	0.059	0.253
	< 0.001	< 0.001	*	*	0.387
Linear Slope	< 0.001	0.0019	< 0.001	0.0492	0.489
	< 0.001	0.0054	< 0.001	*	0.454
	< 0.001	*	< 0.001	*	0.390
Linear Intercept	< 0.001	< 0.001	0.001	< 0.001	0.718
	< 0.001	< 0.001	*	< 0.001	0.656
	< 0.001	< 0.001	*	*	0.397
Maximum Stress	< 0.001	< 0.001	< 0.001	0.487	0.513
	< 0.001	< 0.001	< 0.001	*	0.517
	< 0.001	< 0.001	*	*	0.298
Strain at max. stress	< 0.001	< 0.001	0.0069	< 0.001	0.595
	< 0.001	< 0.001	*	< 0.001	0.539
	< 0.001	< 0.001	*	*	0.236
Strain Energy	< 0.001	< 0.001	0.188	< 0.001	0.408
	< 0.001	< 0.001	*	0.0012	0.395
	< 0.001	< 0.001	*	*	0.275

4 Conclusions

Because principal fibril diameters for pig skin, rabbit skin, and pelican gular sac were all approximately 100 nm, but the extensibility of the gular sac is much higher than that of the other two animal skins, fibril size was not observed to be a prominent factor in the additional extensibility observed in the pelican gular sac relative to regular skin.

Similarly, since the values for fiber thickness were relatively similar for all animals considered, the fiber thickness was not observed to be a prominent parameter causing the skin's exceptional extensibility.

It was observed that fibril radii of curvature in the gular sac material appeared to be smaller than those reported for other animal skins. Although this results in fibril curvature radii less than those documented for the pig, for example, this does not fully explain the higher extensibility seen in pelican skin. It is proposed that this additional extensibility in the transverse direction is a combination of the wavy collagen and corrugated groove crimping structures laying at two different hierarchical levels.

The gular sac skin is suggested to have two layers of functionality based on ESEM observations, rather than acting in correspondence with the three distinctive biological layers.

Age of specimens, at least for birds older than 'infants', was not found to be a strong influence on the gular sac material response with respect to stress and strain metrics or for predictability to the amount of anisotropy exhibited. However, for the very youngest bird, the transverse and longitudinal results were very similar.

Pelican gular sac skin was observed to have significantly lower stress at failure strengths than those reported for rabbit and pig skin. Strains to failure were generally higher than those found for pig and rabbit skin, especially for transverse specimens where flattening of the corrugated surface occurs. The higher strains to failure with lower stresses than observed for the other animals, especially for longitudinally oriented pelican specimens, is evidence of the pelican's skin being naturally more extensible than 'normal' skin.

There is substantial evidence supporting the material's increasing anisotropy with age. All subplots support the 'axis' category as an extensible, but low strength region. For the oldest, largest, bird, trends in material response with dorsoventral location were much more apparent, suggesting that smaller samples from even more finely partitioned pouch sample spaces would likely show these trends even for smaller and younger birds.

Multiple regression analysis for the data from three pelicans of differing ages showed strong correlation between the response parameters and specimen orientation (longitudinal or transverse). Similarly strong correlations were observed between the response parameters and location of the specimen in the pouch – with specimens in the axis and bulk regions similar to each other in most metrics but statistically different from those parameter values for the border regions of the pouch. Estimated age of the birds was well correlated with the response parameters as well, except for heel slope and maximum stress.

5 Appendix: MANOVA results for dorsoventral data.

Figure 42 shows the scatter plots for heel slope (Figure 23). The central green horizontal line identifies the mean value of the group while the vertical span of the diamonds represent the 95% confidence levels of the means. A multiple analysis of variance analysis (MANOVA) produces orientation and location P-values < 0.001 indicating mean heel slope value is strongly correlated with those factors. The P-value for age was 0.849 indicating little correlation in the heel slope mean with the estimated age of the pelican. Figure 42 shows how grouping the bulk and axis location data provides a much clearer correlation of location with the heel slope parameter.

Figures 43 through 46 show the same data for the other factors with orientation and location (border compared to axis and bulk) being strongly correlated with all response parameters.

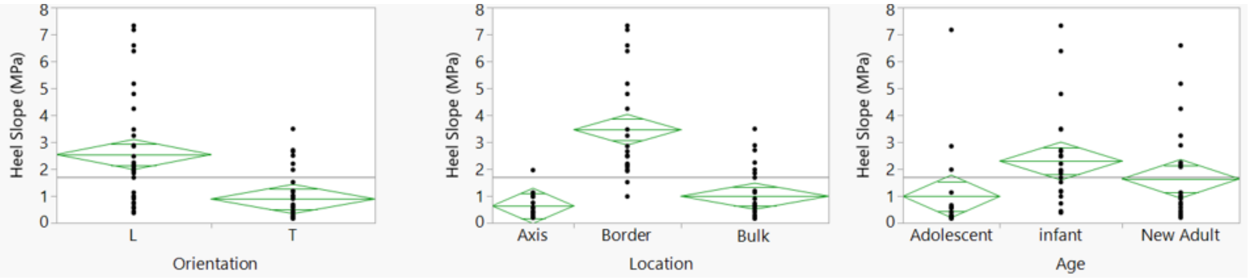

Figure 42: Heel slope scatter charts. P-values for orientation, location, and age are < 0.001, < 0.001, and 0.849, respectively.

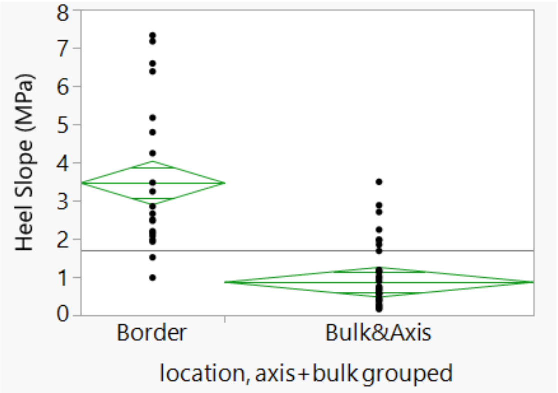

Figure 43: Heel slope scatter plot for location after grouping bulk and axis locations. P-values from MANOVA for P-orientation = 0.0033, P-location < 0.001, and P-age = 0.859.

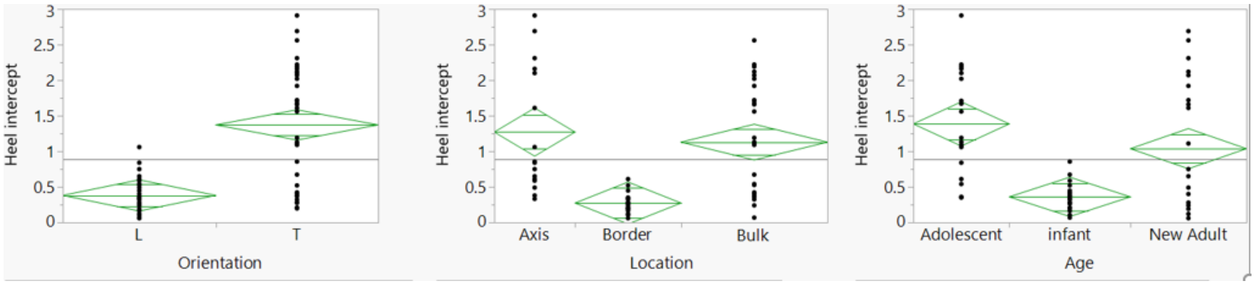

Figure 44: Scatter plots for heel intercept. All P-values were less than 0.001.

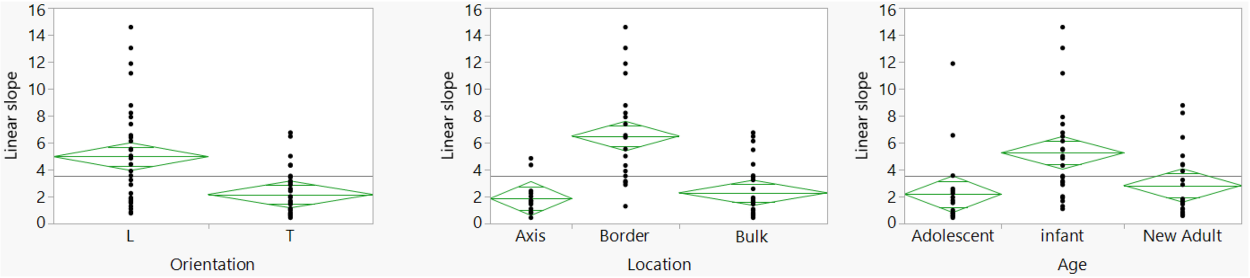

Figure 45: Scatter plots for linear slope. P-orientation < 0.001, P-location < 0.001, and P-age = 0.0024.

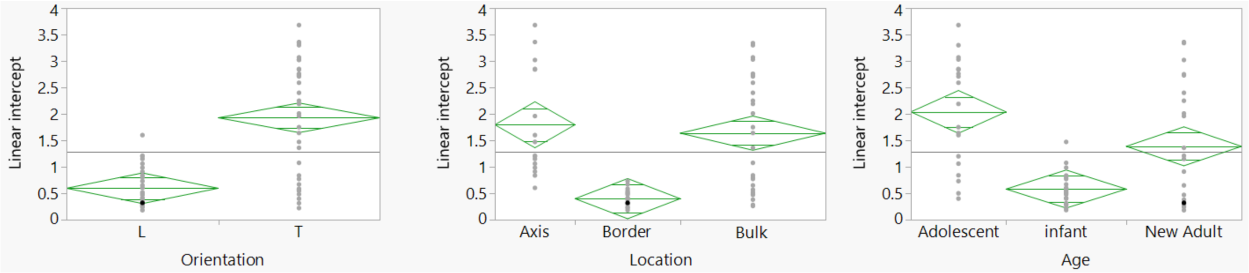

Figure 46: Scatter plots for linear intercept. All P-values < 0.001.

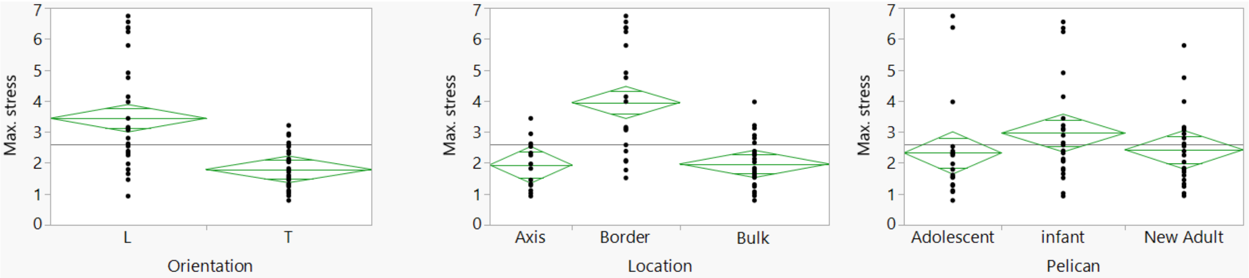

Figure 47: Scatter plots for maximum stress. P-orientation < 0.001, P-location < 0.001, P-age = 0.308.

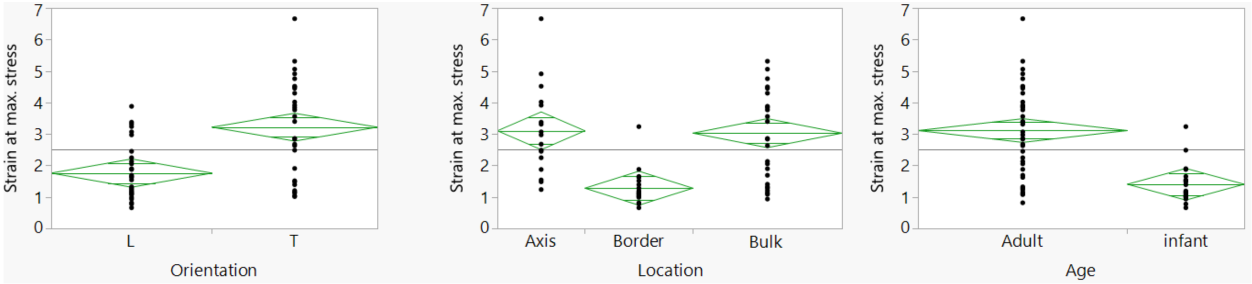

Figure 48: Scatter plots for strain at maximum stress. All P-values < 0.001.

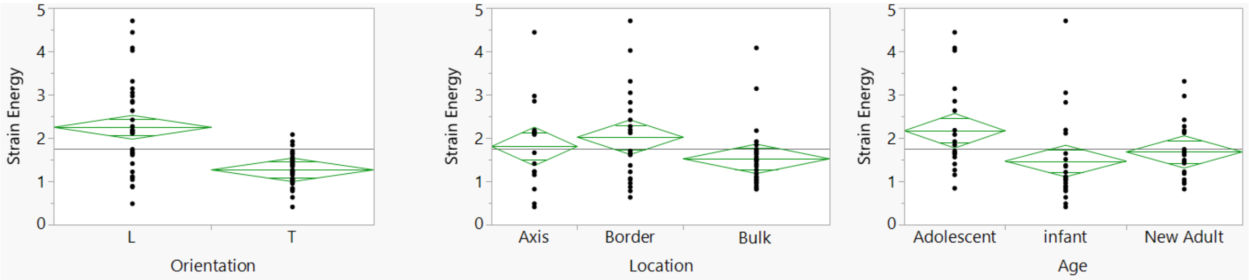

Figure 49: Scatter plots for strain energy. P-orientation < 0.001, P-location < 0.164, and P-age = 0.038.

References

[1] Field DJ, Lin SC, Ben-Zvi M, Goldbogen JA, and Shadwick RE. 2011. Convergent evolution driven by similar feeding mechanics in balaenopterid whales and pelicans. The Anatomical Record 294: 1273–1282.

[2] Field DJ, Campbell-Malone R, Goldbogen JA, Shadwick RE. 2010. Quantitative computed tomography of humpback whale (Megaptera novaeangliae) mandibles: mechanical implications for Rorqual lunge-feeding. Anat Rec 293:1240–1247.

[3] Campbell-Malone, R., 2007. "Biomechanics of North Atlantic right whale bones: mandibular fracture as a fatal endpoint for blunt vessel–whale collision modeling." Ph.D. dissertation, Woods Hole Oceanographic Institution, Woods Hole, MA.449

[4] Vogel S. 2003. Comparative Biomechanics. Princeton, NJ: Princeton University Press. p 365–373

[5] Meyers RA, Myers RP. 2005. Mandibular bowing and mineralization in brown pelicans. Condor 107:445–449

[6] Potvin J, Goldbogen JA, Shadwick RE. 2009. Passive versus active engulfment: verdict from trajectory simulations of lunge-feeding fin whales Balaenoptera physalus. J R Soc Interface. doi: 10.1098/ rsif.2008.0492

[7] Reuge N, Schmidt FM, Le Maoult Y, Rachik M, Abbe´ F. 2001. Elastomer biaxial characterization using bubble inflation technique. I: Experimental investigations. Polym Eng Sci 41:522–531. doi: 10.1002/pen.10749

[8] Sherman VR, Tang Y, Zhao S, Yang W, Meyers MA. 2017. Structural characterization and viscoelastic constitutive modeling of skin, Acta Biomaterialia, Vol. 53, Pages 460-469.

[9] Pissarenko A, Yang W, Quan H, Brown KA, Williams A, Proud W, Meyers MA. 2019. Tensile behavior and structural characterization of pig dermis, Acta Biomaterialia, Vol. 86, Pages 77-95.

[10] Williams TD, Gawlowski PQ, Strickland DM. 1988. Surgical repair of the gular sac of the brown pelican *(Pelecanus occidentalis). J Zoo Anim Med* 19:122-125.

[11] Yang W, Sherman VR, Gludovatz B, Schaible E, Stewart P, Ritchie RO, Meyers MA. 2015. On the tear resistance of skin, Nat. Commun., 6:6649.

[12] Limited, A. (n.d.). Stock Photo - Brown Pelican in breeding colors swallows fish in its pouch.(Pelecanus occidentalis).Bolas Chica Wetlands,California. Retrieved from https://www.alamy.com/brown-pelican-in-breeding-colors-swallows-fish-in-its-pouchpelecanus-image61655990.html

[13] What is a "rorqual" whale? - The Super Fins. (2017, January 11). Retrieved from http://www.thesuperfins.com/what-is-a-rorqual-whale/

[14] JMP®, Version 14.1.0. SAS Institute Inc., Cary, NC, 1989-2019